Università degli Studi di Torino

FACOLTÀ DI SCIENZE MATEMATICHE, FISICHE E NATURALI
Corso di Laurea Magistrale in Fisica Nucleare e Subnucleare

Measurement of the $\chi_b(3P)$ feed-down to $\Upsilon(3S)$

Candidato:
Violetta Cogoni
Matricola 743063

Relatore:
Dott. Stefano Argirò

Anno Accademico 2011–2012

Contents

Abstract

The first evidence of the existence of the $\chi_b(3P)$ meson has been found by the ATLAS Collaboration in 2011. The work presented in this thesis regards the measurement of the fraction of $\Upsilon(3S)$, which was considered feeddown-free until 2011, originating from the $\chi_b(3P)$ decay. This contribution is estimated from the ratio $\sigma(\chi_b(3P) \to \Upsilon(3S) + \gamma)/\sigma(\Upsilon^{inc}(3S))$ of the $\Upsilon(3S)$ produced from the $\chi_b(3P)$ decay and the inclusive $\Upsilon(3S)$ production, that is both the directly produced $\Upsilon(3S)$ and those coming from the $\chi_b(3P)$ decay. The Υ mesons are reconstructed in the leptonic decay $\Upsilon \to \mu^+\mu^-$ and converted photons are used to reconstruct the χ_b candidates. The efficiency is studied via Monte Carlo simulations. This thesis studied $\approx 90\%$ of the data collected by CMS in 2012 in pp collisions at $\sqrt{s} = 8$ TeV. The feed-down contribution in the kinematic range $|y_\Upsilon| < 1.0$, $p_{T,\Upsilon} > 9.5$ GeV and $p_{T,\gamma} > 0.5$ GeV is measured to be $(10.3 \pm 3.1)\%$, where the reported uncertainty is statistical. At the time of the writing of this thesis, no previous experimental studies have been done.

Resùmene

Sa primu evidèntzia de s'esistènzia de su mesone $\chi_b(3P)$ est istada iscoberta dae sa Collaboratziòne ATLAS in su 2011. Su traballu presentadu in custa tesi est a pitzus de sa mesúra de sa fratzione de $\Upsilon(3S)$, chi fiat pensàda chenze *feed-down* fintzas a su 2011, unu produtu de su decadimentu de sa $\chi_b(3P)$. Custu cuntributu est apretàdu impreende sa fratzione $\sigma(\chi_b(3P) \to \Upsilon(3S) + \gamma)/\sigma(\Upsilon^{inc}(3S))$ de is $\Upsilon(3S)$ chi benent de su decadimentu de sa $\chi_b(3P)$ e sa produtzione *inclusive*, est a ischire totu cantu funti is $\Upsilon(3S)$. Sa ricostrutzione est istada fata cun is mesones Υ decadende in duos leptones $\Upsilon \to \mu^+\mu^-$ e, po sa ricostrutzione de su mesone χ_b, cun is fotones cunvertidos. S'efitzèntzia esti istudiada dae sa fingidura Monte Carlo. Custa tesi istudiat su 90% de su campione regòllidu dae s'esperimentu CMS in su 2012 in collisiones pp a $\sqrt{s} = 8$ TeV. Su contributu in su tretu chinemàticu $|y_\Upsilon| < 1.0$, $p_{T,\Upsilon} > 9.5$ GeV e $p_{T,\gamma} > 0.5$ GeV est istadu apretadu e bàlet $(10.3 \pm 3.1)\%$, in ue s'errore impreadu est s'istatìsticu. Candu custa tesi est istetia iscrita, no bi fiant galu istudios isperimentales.

Introduction

The production of heavy quarkonium states at hadron colliders is a topic of considerable experimental and thoretical interest. The CMS design allows to study such states with great precision. In particular, this thesis presents the measurement of the fraction of $\Upsilon(3S)$ originating from the radiative decays of $\chi_b(3P)$ mesons, that have been discovered at LHC (by ATLAS Collaboration) in 2011. The importance of this work is related to polarization and producion cross-section measurement.

The first chapter is a summary of the main theories at the base of heavy quarkonia production, and an overview of the previous studies regarding P-wave bottomonium states.

The second chapter briefly illustrates the Large Hadron Collider, while the third chapter describes the Compact Muon Solenoid experiment, its tasks and the main details of its subdetectors, which can be useful to understand how the measurement has been performed.

The fourth chapter describes in detail all the analysis, from the choice of the selection cuts to the approximations introduced, to the achievement of the result.

Finally, the fifth chapter contains the conclusions that can be drawn from this work.

The last pages report the main bibliography references used for the theoretical models presented, for the detailed description of the detector, in addition to all the papers/articles that have been precious for a deeper understanding of the subject.

Chapter 1

Theory overview and previous studies

Quarkonia are bound states composed of a quark and an antiquark. Each quarkonium state can be named with his standard spectroscopic notation, that is $n^{2S+1}L_J$: n is the radial quantum number, S the total spin of the $q\overline{q}$ pair, L the orbital angolar momentum ($L = 0 \rightarrow S$, $L = 1 \rightarrow P$, $L = 2 \rightarrow D$) and $J = L + S$ the total angular momentum. The quark and the antiquark, each having spin 1/2, can have parallel or antiparallel spin. If the spins are aligned, their total spin is $S = 1$ that can have three spin projections ($S_z = -1, 0, +1$), and this state is called "triplet"; if their spins are opposed, they represent the "singlet"$S \equiv S_z = 0$. Quarkonia states can also be classified by J^{PC}, where $P = (-1)^{L+1}$ is the "parity"and $C = (-1)^{L+S}$ is the "c-parity"(charge conjugation). In this thesis, the notation $[name]_J(nL)$ is widely used.

1.1 Theory of Charmonium Production and Decay

Systems made up of quarks having a mass larger than the QCD confinement scale $\Lambda_{QCD} \simeq 300$ MeV, like the charm ($m_c \simeq 1.4$ GeV) and the bottom ($m_b \simeq 4.5$ GeV), are called "heavy quarkonia". Even though the top mass is larger than Λ_{QCD} ($m_t \simeq 175$ GeV), $t\bar{t}$ pairs are not known to form bound states, because top quarks have a short life-time and they decay before bound states can be formed. The lower-mass states of heavy quarkonium resonances are rather stable particles: their mass is below the threshold for open heavy

flavoured mesons pair production, so their decay modes are electromagnetic or OZI-suppressed. This implies that all charmonium and bottomonium excited states below the open charm/bottom threshold have narrow widths, ranging from a few tenths keVs to a few dozen MeVs. The bottomonium spectrum is shown in Fig.1.1.

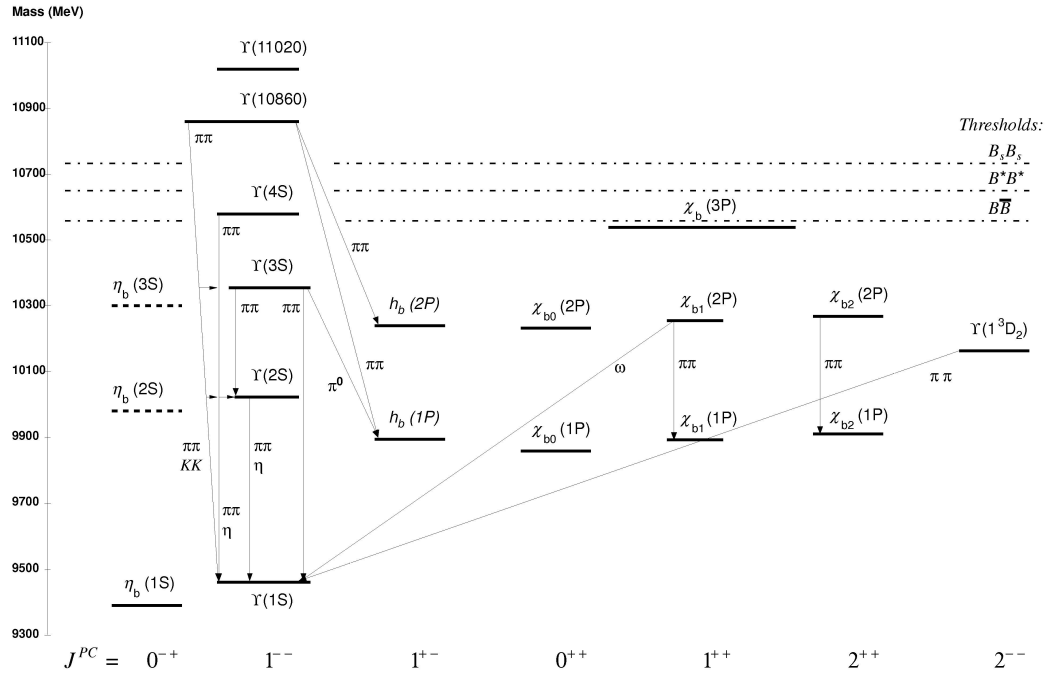

Figure 1.1: Bottomonium spectroscopy diagram.

The spectroscopy of quarkonia can be described assuming the existance of a binding potential. A well known example is the Cornell potential, consisting of a Coulomb-like term, $V \sim 1/r$, to account for gluon-exchange between the two quarks at small distances ($r \sim 0.1$ fm), and of a linear potential, $V \sim r$, to account for quark confinement at large distances ($r \sim 1$ fm):

$$V(r) = -\frac{4}{3}\frac{\alpha_s}{r} + k^2 r. \tag{1.1}$$

In Eq.1.1, α_s is the strong coupling constant , $\frac{4}{3}$ is a colour factor and r is the distance between the two quarks. The solutions of the Schrödinger equation with this functional form of $V(r)$ gives a good account of the full quarkonium spectroscopy.

With regard to the mechanisms of quarkonium production, these are still matter of research. Earlier theories ruled out the hypoteses of electromagnetic production via $q\overline{q}$ annihilation *à la* Drell Yan or into a gluon. Electromagnetic processes can't be the main mechanisms of production, since comparing $\pi^- \; N \rightarrow q\overline{q} \; X$ and $\pi^+ \; N \rightarrow q\overline{q} \; X$ cross sections one should observe a factor 4 in the ratio, since $\sigma \propto (Q_q)^2$ (where Q_q is the charge of the

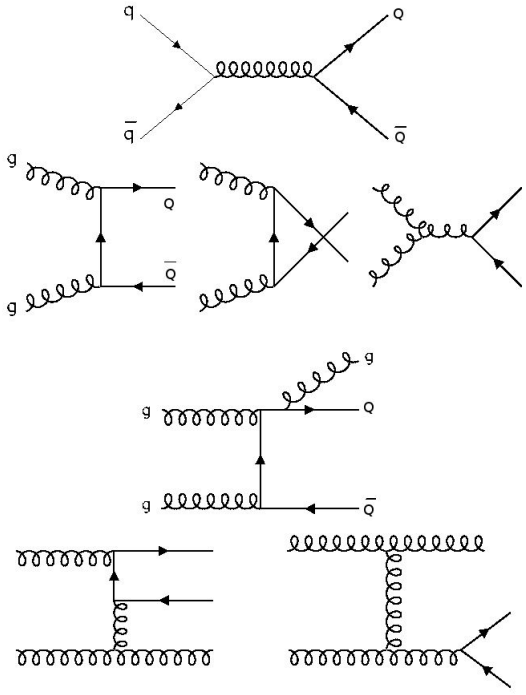

Figure 1.2: Main Feynman diagrams contributing to quarkonium production.

quark q) which is not observed. Likewise, $q\overline{q}$ annihilation into a gluon was rejected as main mechanism of production comparing heavy quarkonia production in pp and $p\overline{p}$ low energy collisions. One should observe a suppression of a factor 5-10 in pp with respect to $p\overline{p}$ production, since $\overline{p}$ has a valence quark, but the experiments observed a far less gap. So heavy quarkonia production must proceed via gluon fusion or gluon fragmentation. Fig.1.2 shows the main Feynman diagrams that contribute to heavy quarkonia production.

In heavy quarkonium decay and production, both "short distance"and "long distance"terms are involved. One the one hand, the heavy-quark mass m_Q is much larger than Λ_{QCD} and the transverse momentum p_T can be larger than Λ_{QCD}, too. On the other hand, the momentum of the heavy quark or antiquark in the quarkonium rest frame is of the order of $m_Q v$, and the binding energy of the $q\overline{q}$ system is of the order of $m_Q v^2$, where v is the velocity of the heavy quark/antiquark in the quarkonium rest frame ($v^2 \approx 0.1$ for the Υ). In order to employ perturbative methods for the study of quarkonium production, it's important to demonstrate the validity of the

"factorization"approach, *i.e.* the separation between short-distance/high-momentum/perturbative effects and the long-distance/low-momentum/non perturbative effects. Several models were developed over the years to describe theoretically or phenomenologically the quarkonia production mechanism and such models have been tested at the end of the twentieth-century on data collected at Tevatron. Most important among these are the colour-singlet model (CSM, 1975), the colour evaporation model (CEM, 1977), the nonrelativistic QCD factorization approach (NRQCD, 1986), and the fragmentation-function approach (pQCD, 2005). They are illustrated below and further details can be found here [3].

1.1.1 The Colour-Singlet Model, CSM

The Colour-Singlet Model was proposed shortly after the discovery of the J/ψ. The fundamental idea is that when the $q\overline{q}$ pair evolves into quarkonium, it must have the same spin and the same angular momentum as the bound state; moreover, it must be produced in a colour-singlet state. In this model, the production rate for a specific quarkonium state is obtained comparing the theoretical expressions for $q\overline{q}$ wave function and its derivative, calculated at zero separation, with the experimental observations.

The CSM was successful in predicting quarkonium production rates at relatively low energy, so it was widely used till the nineties, when it was definitively condemned by collider experiments. Indeed, the production cross section of J/ψ at Tevatron was 50 times larger than CSM predictions. Recently, it has been found that, when considering next-to-leading-order (NLO) and next-to-next-to-leading-order (NNLO) terms in α_s, very large corrections appear, so this could put back into play the CSM (even if it is unclear if the perturbative expansion in α_s converges).

1.1.2 The Colour Evaporation Model, CEM

In the Colour Evaporation Model it is assumed that $q\overline{q}$ pair evolves into a quarkonium every time that the invariant mass of the heavy quark pair is less than twice the mass of the lighter open-flavour heavy meson, no matter what is the colour or the quantum numbers of the $q\overline{q}$. For charmonium, *e.g.*, the threshold is 2 m_D. The heavy quarkonium then neutralizes its colour by the emission of one or more gluons – thus it's known as "colour evaporation". Furthermore, the $q\overline{q}$ pair evolves in a final-state quarkonium H with a probability F_H that is energy-momentum and process independent,

and that includes both direct and indirect production from radiative and hadronic decays. So, once F_H is determined through the data in a certain process and in certain energy-momentum conditions, it can be used for other processes and other kinematic conditions.

This model predicts that all produced states are unpolarized. One weak point of CEM is that it lacks a solid theoretical ground. Its predictions describe the CDF data for J/ψ, $\psi(2S)$ and χ_{cJ} at $\sqrt{s} = 1.8$ TeV very approximately. For example, the fits to the J/ψ yield are bad, with a $\chi^2/n_{d.o.f.}$ that varies from 2 – 4.5 to even 7 – 8.

1.1.3 The Nonrelativistic QCD, NRQCD

The NRQCD succeeds in reproducing full QCD dynamics accurately at momentum scales of order $m_Q v$ and smaller, where v is the heavy quark velocity in the $Q\overline{Q}$ pair in the center-of-mass frame (*e.g.* $v^2 \approx 0.3$ for charmonium and $v^2 \approx 0.1$ for bottomonium). Processes involving momentum scales of order m_Q or larger can affect lower momentum processes, and they are taken into account through the short-distance coefficients of the operators that appear in the NRQCD action.

In the NRQCD factorization approach, the inclusive cross section for direct production of a quarkonium state H is written as a sum of products of short-distance coefficients and non-perturbative matrix elements, that describe the probability for a $Q\overline{Q}$ pair to evolve in the quarkonium state:

$$\sigma(H) = \sum_n C_{[n]}^{Q\overline{Q}} \left\langle O_n^H \right\rangle \tag{1.2}$$

where $C_{[n]}^{Q\overline{Q}}$ are the perturbative, short-distance coefficients, and the matrix elements $\left\langle O_n^H \right\rangle$ are the vacuum-expectation values of four-fermions operators in NRQCD. In Eq.1.2, the n states can be both colour-singlet and colour-octet states (here's why NRQCD is also known as Colour Octet Model) and correspond to various angular-momentum states of the $Q\overline{Q}$ pair. If one excludes all the colour-octet contributions from the Eq.1.2, then one obtains the Colour Singlet Model (see 1.1.1).

The matrix elements are process independent, and this increases the predicting power of nonrelativistic QCD. They should be determinated phenomenologically or calculated in lattice simulations, but at present they can only be found from phenomenology.

The NRQCD describes reasonably well the experimental data; for example the fits to the CDF J/ψ yield are very good, with a $\chi^2/n_{d.o.f.} \approx 1$.

Nevertheless, the NRQCD is often criticized for it has a large number of parameters, which makes the theory less predictive.

1.1.4 Fragmentation function approach

This approach depicts hadron formation by the fragmentation of a jet produced by a parton with high p_T, and it is believed to be the dominant mechanism of quarkonium production at high transverse momentum. This mechanism is described by a universal fragmentation function that represents the probability for a parton to fragment into a hadron carrying a certain fraction of the parent parton's momentum.

This procedure considers the convolution of parton production cross section with light-cone fragmentation functions in order to obtain the inclusive quarkonium production cross section.

At the leading power in m_Q/p_T, the contribution to the cross section is given by the production of a single parton at a distance scale of order $1/p_T$ which fragments into a heavy quarkonium, while at the first subleading power in m_Q/p_T, it's given by the production of a $Q\overline{Q}$ pair in a vector- or axial-vector state, at a distance scale of order $1/p_T$, which then fragments into heavy quarkonium.

1.2 The χ_b States

For what concerns the $b\bar{b}$ system, the P-wave states are the $\chi_b(nP)$. The $\chi_b(1P)$ and $\chi_b(2P)$ were first observed at the Columbia University (CUSB Collaboration) in 1983 and 1992 respectively, while the $\chi_b(3P)$ was first observed by ATLAS at LHC in December 2011[4]. The masses and the branching ratio for the radiative decay are reported in Tab. 1.1.

As one can see, the mass splitting between states with the same n and different J (hyperfine split, of the order of magnitude of ten MeV) is very small compared to the masses themselves, of the order of magnitude of ten GeV . For what concerns the $\chi_b(3P)$, the barycenter of mass of the triplet has been reported, since the single spin states could not be resolved experimentally.

Observing the second column in Tab. 1.1, can be seen that for each nP triplet, the $J = 0$ state is the one with the smallest branching ratio for the radiative decay. So, as can be observed from experiments, the $J = 1$ and $J = 2$ spin states will have a greater yield.

	Mass (MeV)	BR($\chi_b \to \Upsilon(1S) + \gamma$)
$\chi_{b0}(1P)$	$9859.44 \pm 0.42 \pm 0.31$	$< 6\%$
$\chi_{b1}(1P)$	$9892.78 \pm 0.26 \pm 0.31$	$35 \pm 8\%$
$\chi_{b2}(1P)$	$9912.21 \pm 0.26 \pm 0.31$	$22 \pm 4\%$
$\chi_{b0}(2P)$	$10232.5 \pm 0.4 \pm 0.5$	$0.9 \pm 0.6\%$
$\chi_{b1}(2P)$	$10255.46 \pm 0.22 \pm 0.5$	$8.5 \pm 1.3\%$
$\chi_{b2}(2P)$	$10268.65 \pm 0.22 \pm 0.5$	$16.2 \pm 2.4\%$
$\chi_b(3P)$	$10539 \pm 4 \pm 8$	(unknown)

Table 1.1: Masses and branching ratios for the various $\chi_b(nP)$ states.

1.3 Previous studies on χ_b states

While $\chi_b(1P)$ and $\chi_b(2P)$ are well known since long and both their leptonic and hadronic decays have been studied, the $\chi_b(3P)$ is a recent discovery so it shows many aspects to be determined. The reason why $\chi_b(3P)$ was not found before consists in the fact that, in e^+e^- colliders, χ states cannot be directly produced, thus it is necessary to study the radiative decay from a higher-mass vector meson. Looking at bottomonium spectroscopy diagram (see Figure 1.1), the $\Upsilon(4S)$ is the lowest-mass state that allows $\chi_b(3P)\gamma$ decays. Unfortunately, $\Upsilon(4S)$ is massive enough to be above the threshold to decay into $B\overline{B}$ or B^+B^-, which are the dominant mechanisms of decay.

The $\chi_b(3P)$ was first observed by ATLAS Collaboration in December 2011[4] through its radiative decays in $\Upsilon(1S) + \gamma$ and in $\Upsilon(2S) + \gamma$. A few months later, the D0 Collaboration confirmed the result, though in the only channel $\Upsilon(1S) + \gamma$[5].

In both experiments the χ_b states are reconstructed with $\Upsilon \to \mu^+\mu^-$ and with the photon conversion in a pair e^+e^-. ATLAS Collaboration reconstructed the photon by direct calorimetric measurement, too, confirming the $\chi_b(3P)$ discovery.

The ATLAS Collaboration used a data sample recorded in 2011 LHC pp collision run at a centre-of-mass energy $\sqrt{s} = 7$ TeV. To reconstruct the Υ, the di-muon must satisfy some quality requirements: muon pairs with opposite charge sign are selected, than they are fitted to a common vertex. The di-muon candidate also must have $p_T > 12$ GeV and $|y| < 2.0$. Concerning the converted photons, each conversion electron track must have $p_T \geq 500$ MeV and each converted photon candidate must have $|\eta| < 2.30$.

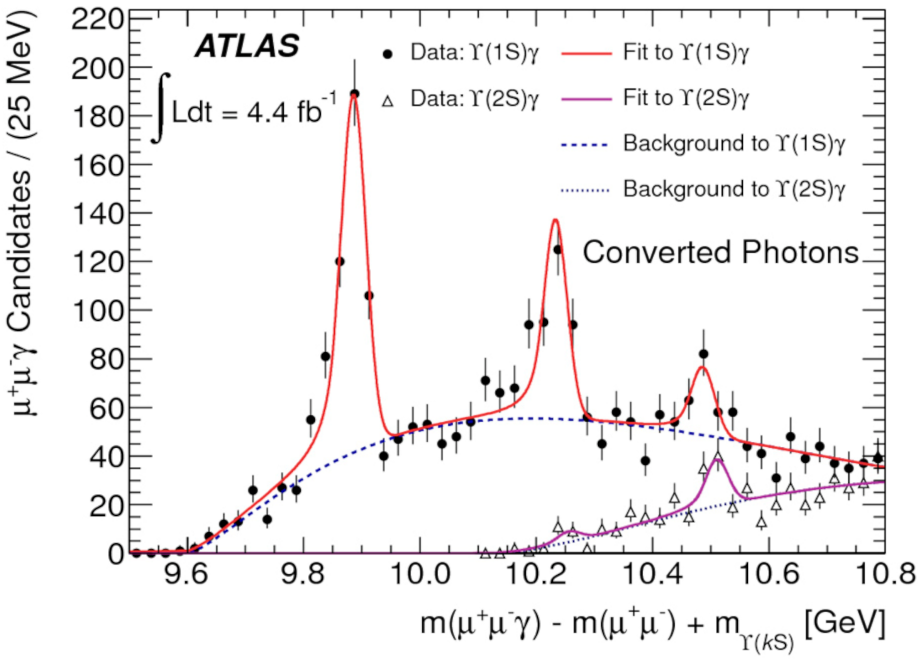

Figure 1.3: Invariant mass $m_{\mu\mu\gamma} - m_{\mu\mu} + m_{\Upsilon_{PDG}}$ obtained in ATLAS experiment and its fit.

The χ_b candidate is then selected associating a reconstructed Υ with a reconstructed photon. The χ_b invariant mass is calculated as $m(\mu^+\mu^-\gamma) - m(\mu^+\mu^-) + m(\Upsilon_{PDG})$ rather than simply $m(\mu^+\mu^-\gamma)$, because the difference $m(\mu^+\mu^-\gamma) - m(\mu^+\mu^-)$ is not affected by the effect of $\Upsilon \to \mu^+\mu^-$ finite mass resolution. Finally, a fit is performed on the spectrum using two Crystal Ball functions for each $\chi_b(nP)$ peak (for $n = 1, 2$, $J = 0$ radiative decay is suppressed with respect to $J = 1, 2$, so its contribution is omitted). This invariant mass distribution is shown in Fig. 1.3. The Crystal Ball function is essentially composed of a Gaussian peak and a power-law low-end tail, and will be discussed in 4.3.2.

The D0 Collaboration used the same particle reconstruction method as ATLAS. Because of the different experimental layout, also the requirements to be fulfilled by the selected particles are different. To reconstruct the converted photon, the conversion pair invariant mass must satisfy $M_{ee} < 80$ MeV. Furthermore, each muon must have $p_T > 1.5$ GeV and the transverse momentum of the χ_b candidate must be greater than 5 GeV. The fit to the invariant mass distribution is again performed using Crystal Ball functions

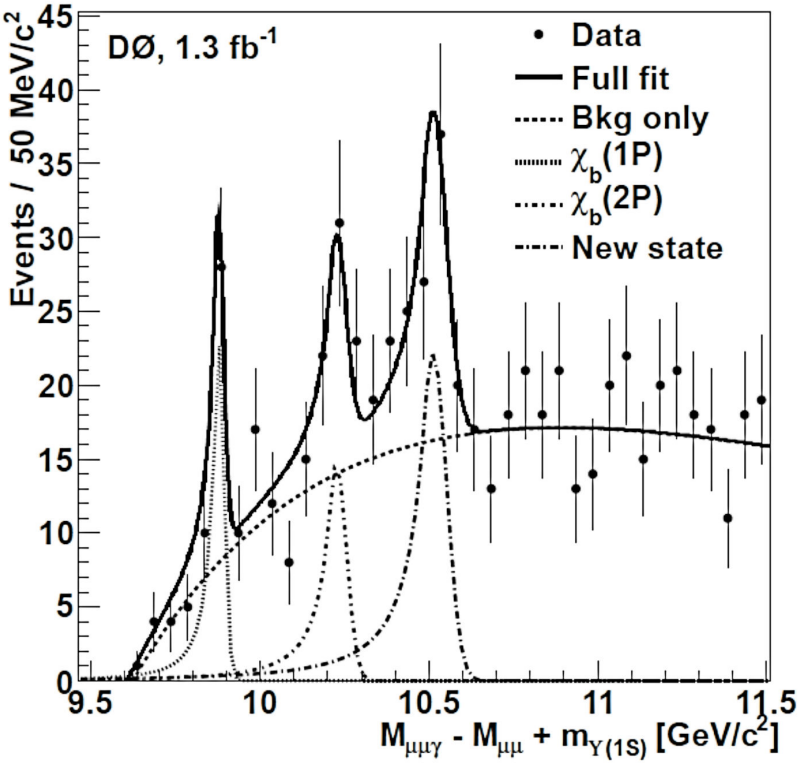

Figure 1.4: Invariant mass $m_{\mu\mu\gamma} - m_{\mu\mu} + m_{\Upsilon_{PDG}}$ obtained in D0 experiment and its fit.

to fit the signal.

Since, in both cases, the mass resolution is not good enough to perceive the hyperfine splitting, only the baricenter mass of the $\chi_b(3P)$ is measured. ATLAS measured $m_{\chi_b(3P)} = 10.539 \pm 0.004(\text{stat.}) \pm 0.008(\text{syst.})$ GeV, and D0 found $m_{\chi_b(3P)} = 10.551 \pm 0.014(\text{stat.}) \pm 0.017(\text{syst.})$ GeV, that is compatible with the previous result.

In 2012, CMS Collaboration succeeded in observing the $\chi_b(3P)$ through its radiative decay in $\Upsilon(1S) + \gamma$, $\Upsilon(2S) + \gamma$ and $\Upsilon(3S) + \gamma$, reconstructing the candidates in a similar way to ATLAS and D0 Collaborations.

1.4 Current theoretical predictions

While the splitting of the $J = 0, 1, 2$ states in the $\chi_{b,J}(1P)$ and $\chi_{b,J}(2P)$ has been experimentally determined, there is still no data for the splitting in the $\chi_{b,J}(3P)$. Several theoretical works predict the mass splitting for the $3P$ triplet, and the most recent of this works uses four different potential models. Finally this theoretical work predicts the masses m_J of the triplet of $\chi_{b,J}(3P)$ to be: $m_0 = (10502 \pm 10)\ MeV$, $m_1 = (10524 \pm 10)\ MeV$ and $m_2 = (10539 \pm 10)\ MeV$. Note that the $J = 2$ state would be just $20 \pm 10\ MeV$ below the B^+B^- threshold. Further details can be found in [12].

The study of P-wave $q\overline{q}$ prompt production shows interesting aspects. Besides being an important test of QCD and quarkonium production mechanisms, it shows unexpected behaviours: ${}^3S_1$ states (like the Υ) are produced via 3-gluon processes, while ${}^3P_0$ and ${}^3P_1$ via 2-gluon processes, therefore one can suppose that the production rate must be larger for P-wave states than for S-wave states, causing feed-down to be a substantial ${}^3S_1$ production source. Moreover, ${}^3P_1$ production via 2-gluon processes is suppressed by Landau-Yang theorem, and spin counting suggests a ${}^3P_2$ production with respect to ${}^3P_1$ in a 5 : 3 ratio. These prediction are unsupported by any evidence and actually contradicted by experimental data.

Chapter 2

The Large Hadron Collider

As usual, a few words are going to be spent about the Large Hadron Collider (LHC) experiments and the CMS experiment in particular. The Large Hadron Collider is a hadron accelerator built by the European Organization for Nuclear Physics (CERN) from 1998 to 2008.

The LHC was designed to fill the gaps of the Standard Model: to find the Higgs boson (hypotized in 1964), the bedrock of the Higgs mechanism; to look for super-symmetric particles; to study the differences between matter and antimatter; in general, to study particle physics at the energy scale of TeVs.

The pursuit of these objectives imposed some technical features:

- Hadron collider: in hadronic collisions, the exact energy of interacting partons is unknown. In principle, in a $\sqrt{s} = 14$ TeV pp collision, each parton carries a fraction $x \sim 0.15 - 0.2$ of the proton momentum, so the energy range $\sqrt{\hat{s}} = \sqrt{x_1 x_2 s} \simeq 1$ – 2 TeV can be probed. With respect to lepton colliders, a hadron collider has the advantage that proton acceleration to great energies is easier. Indeed, synchrotron radiation is less important for heavier particles, since the radiated power is proportional to $1/m^4$;

- Proton-proton collisions: processes like Higgs production are dominated by gluon fusion, hence the cross section is approximately the same for pp and $p\overline{p}$ collisions, but high intensity beams of protons are easier to accumulate;

- High luminosity: the event rate R for a certain process is given by $R = \sigma\mathcal{L}$ where σ is the cross section and $\mathcal{L}$ is known as luminosity,

and it represents the number of collisions per unit of time and per cross-sectional area of the beams:

$$\mathcal{L} = \frac{n \cdot f \cdot N_1 N_2}{A} \cdot F \tag{2.1}$$

where f is the frequency of revolution around the rings, n is the number of bunches in the beam, N_1 and N_2 are the number of protons per bunch, A is the transverse area of the proton beams and F is the geometric luminosity reduction factor ($\sim 0.8 - 0.9$), due to the crossing angle between the two beams at the interaction point. Processes like those involving the Higgs boson have a low cross section, thus the LHC must compensate with a very high luminosity, reached through a high number of bunches per beam and a very short bunch crossing interval.

Until now, the LHC is the world's largest and highest-energy particle accelerator. Indeed, it consists of a 27 km tunnel that crosses the frontier between Swiss and France, at about 100 m underground. It was conceived to study proton-proton collisions at a centre-of-mass energy of 14 TeV and luminosity up to 10^{34} cm^{-2} s^{-1}, and to study lead-lead collisions at 5.5 TeV per nucleon with luminosity up to 10^{26} cm^{-2} s^{-1}[6].

The first proton-proton beams circulated successfully on September 2008 but unfortunately a serious fault caused the damaging of a number of superconducting magnets, forcing a long technical intervention. The LHC activity restarted on November 2009 and, after few pilot runs at energies of 450 GeV and 1.18 TeV per beam, the energy was ramped up to 3.5 TeV and first collisions took place on 30$^{\text{th}}$March 2010 at a centre-of-mass energy of 7 TeV. This was the highest energy ever reached at a particle collider.

The LHC has operated through the rest of 2010 at the same beam energy of 7 TeV increasing the instantaneous luminosity $\mathcal{L}$ either by increasing the current intensity of the beam or increasing the number of bunches per beam.

With this energy, about 44 pb^{-1} of integrated luminosity were delivered during 2010 with a maximum instantaneous luminosity of $2 \cdot 1032$ cm^{-2}s^{-1}, obtained with start-up conditions: 368 bunches per beam with collisions every 150 ns.

According to the plans, LHC has run with $\sqrt{s} = 8$ TeV center of mass energy for the whole 2012, and currently the machine is in shut down for at least two year to technically prepare for running at $\sqrt{s} = 14$ TeV. During this time the various detectors installed at LHC may upgrade their subdetectors systems to improve their performance in view of the higher-energy, higher-luminosity runs.

The LHC is the final stage of a succession of accelerators shown in Figure 2.1. Each accelerator boosts the speed of a beam of particles, before injecting it into the next one in the sequence.

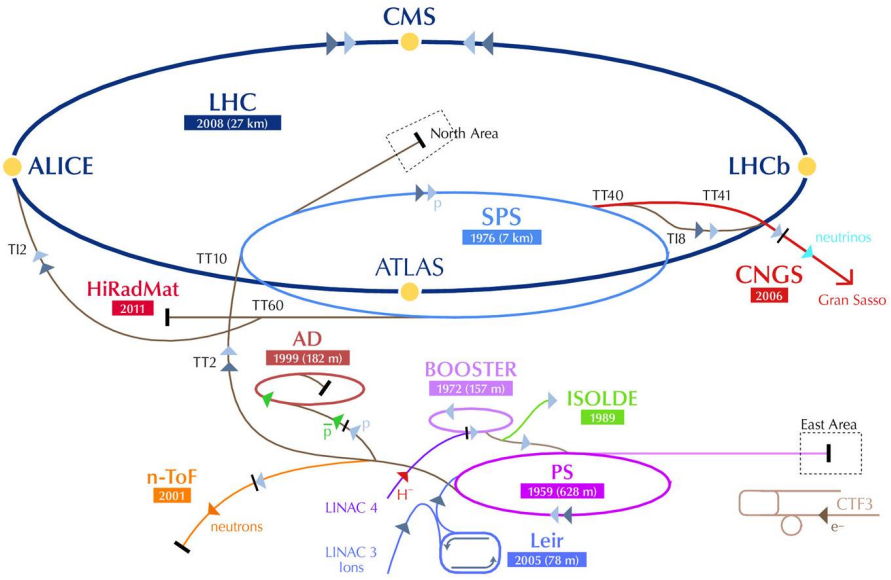

Figure 2.1: CERN Accelerator Complex

When studying proton-proton collisions, the protons are obtained removing the electrons from hydrogen atoms. They are first accelerated in the linear accelerator (LINAC2) and in the Proton Synchrotron (PS), then in the Super Proton Synchrotron (SPS), before finally reaching the two rings of the Large Hadron Collider (LHC). Protons circulate in the LHC for 20 minutes before reaching the maximum speed and energy.

When studying lead-lead collisions, lead ions for the LHC start from a source of vaporised lead and enter LINAC3 before being collected and accelerated in the Low Energy Ion Ring (LEIR). They then follow the same route to maximum acceleration as the protons.

The Large Hadron Collider hosts four main experiments; each one has a different subdetector scheme, specialised to study a particular area of particle physics.

- ATLAS (A large Toroidal Lhc ApparatuS) is a general-purpose detector. It is built with a cylindrical geometry surrounding the beam pipe. To bend the particle trajectories it uses a toroidal magnetic

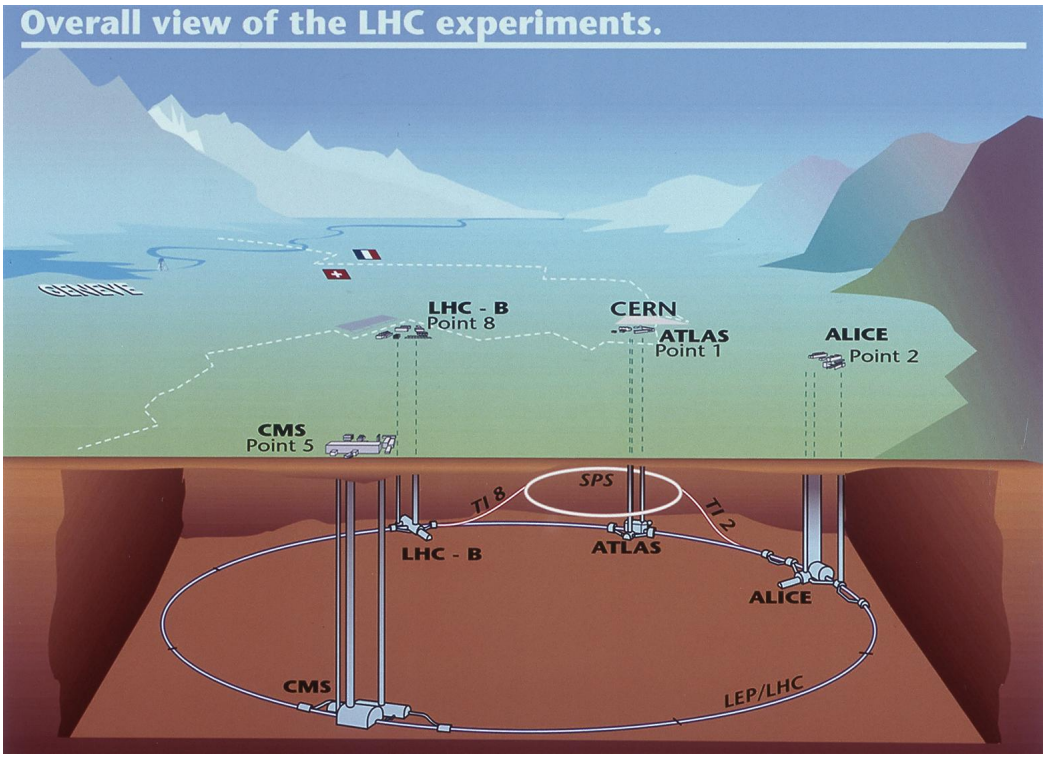

Figure 2.2: An overview of the LHC area and of the interaction points.

ffield produced by three sets of air-core toroids complemented by a small solenoid in the inner region;

- CMS (Compact Muon Solenoid) is a general-purpose, detector like ATLAS, and has a cylindrical geometry, too. It differs from ATLAS because it bends the charge particle trajectories using a magnetic field generated by the world's largest superconducting solenoid;

- LHCb (Large Hadron Collider beauty experiment) doesn't surround the entire collision point, but stretches for 20 m along the beam pipe covering the forward region. It studies the heavy quark and heavy meson physics with a particular attention to the b quark and its mesons;

- ALICE (A Large Ion Collider Experiment) is a heavy-ion dedicated detector. It has been conceived to study the physics of strongly interacting matter at extreme energy densities, where the formation of a new phase of matter, the quark-gluon plasma, is expected. The exis-

tence of such a phase and its properties are key issues in QCD for the understanding of confinement and of chiral-symmetry restoration.

Furthermore, at $\sim$ 100 m from the interaction points of CMS and ATLAS, two forward detectors are placed, TOTEM (TOTal cross section, Elastic scattering and diffraction dissociation Measurement) and LHCf (LHC forward experiment). They are conceived to study the physics processes in the region very close to the particles beam, at extremely low angles (forward region).

Chapter 3

The Compact Muon Solenoid experiment

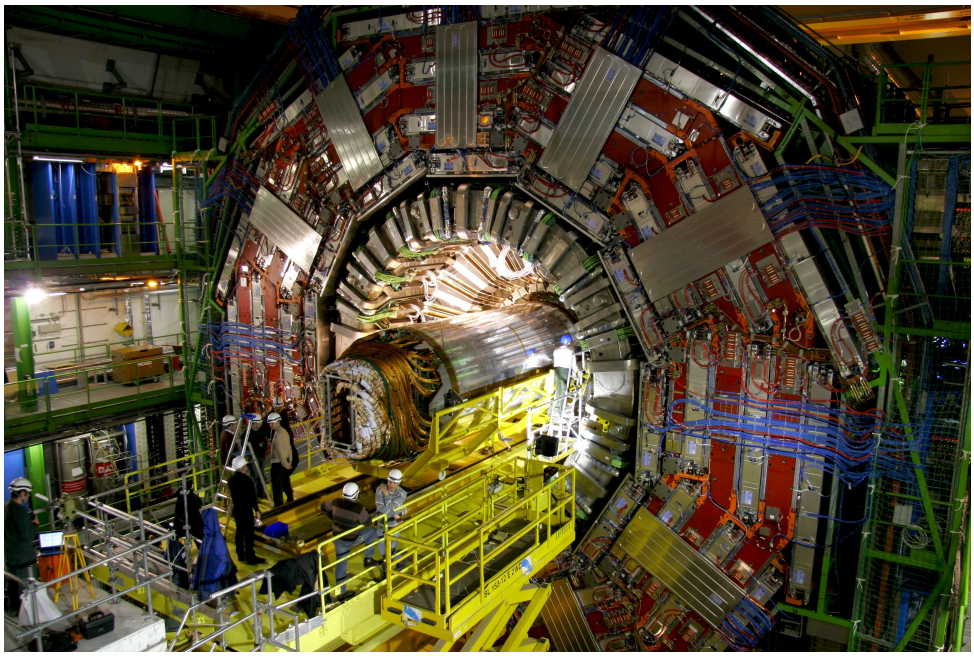

Figure 3.1: An image of the CMS experiment before closing.

The Compact Muon Solenoid (CMS) studies proton-proton collisions to investigate a wide range of physical processes, such as the search for the Higgs boson, extra dimensions, and particles that could constitute dark matter. To pursue these aims, the apparatus must satisfy the following requirements:

- good muon identification and momentum resolution over a wide range of momenta in the region $|\eta| < 2.5$. The charge of muons should be determined without ambiguity for momenta up to 1 TeV;
- good dimuon mass resolution (about 1% at 100 GeV);
- good charged-particle momentum resolution and reconstruction efficiency in the tracking system, together with efficient triggering and offline tagging of tau leptons and b-jets;
- good energy resolution in electromagnetic calorimeters, good diphoton and dielectron mass resolution, good measurement of the direction of photons and correct localization of the primary interaction vertex, efficient π^0 rejection and efficient photon and lepton isolation at high luminosities;
- good missing energy and dijet mass resolution, using hadronic calorimeters with a large hermetic geometric coverage ($|\eta| < 5$) and with fine lateral segmentation.

The CMS detector consists of a series of subdetectors which can measure energy, momentum and position of leptons, photons and hadrons. A sectional view of the detector is shown in Figure 3.2.

The detector structure consists of cylindrical barrel and two endcaps, that host a silicon-based tracking system, a homogeneous scintillating-crystals-based electromagnetic calorimeter, a sampling hadronic calorimeter, a solenoid and various muon chambers. The overall length is 21.6 m, the diameter 14.6 m and the total weight about 12500 tons. The thickness of the detector in radiation lengths is greater than 25 X_0 for the electromagnetic calorimeter, and the thickness in interaction lengths varies from 7 to 11 λ_I for the hadronic calorimeter, depending on the η region.

3.1 The Superconducting Magnet

The CMS magnet is the central device around which the experiment is built and has been designed to reach a 4-T field in the inner region. It reaches 6 m in diameter and is 12 m long. Its aim is to bend the trajectories of the particles emerging from the vertex where the collisions take place. The magnet coil hosts the tracking system, the hadronic and the electromagnetic calorimeters, while its return yoke contains the muon detectors. It operates

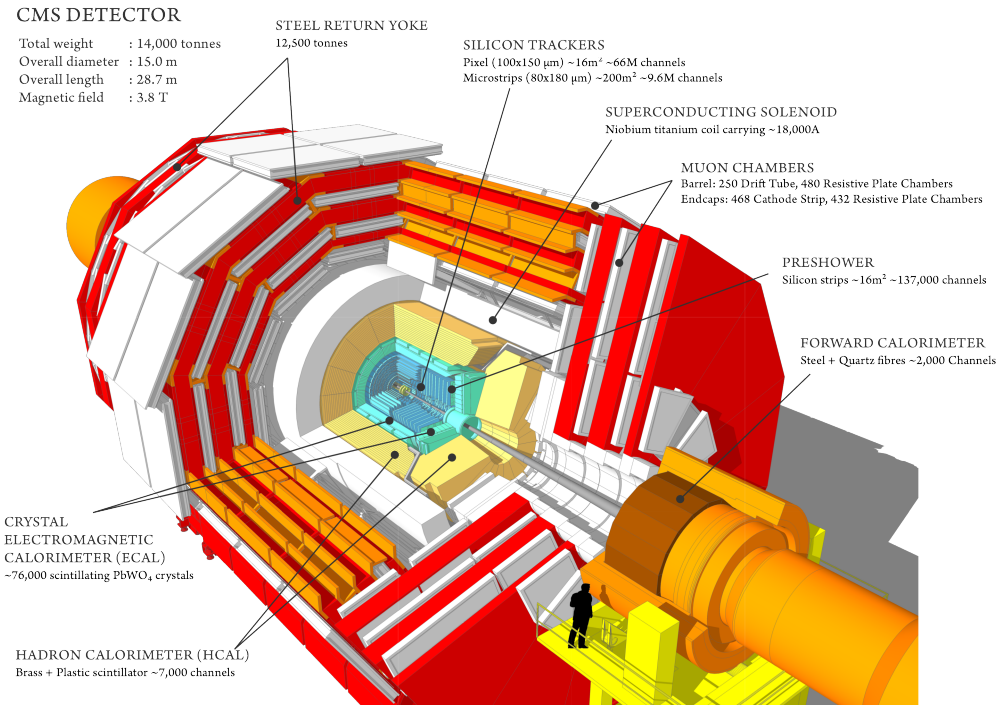

Figure 3.2: Sectional view of the CMS detector. The LHC beams travel in opposite directions along the central axis of the CMS cylinder colliding in the middle of the CMS detector.

at a temperature of 4 K, ensured by a helium cooling system. At such temperatures, the $NiTb$ cable becomes superconducting, allowing a 20 kA current to flow without appreciable loss.

An enormous vacuum cylinder contains the magnetic coil, while the return yoke is placed outside the cylinder. The return yoke is made of iron and consists of five barrel layers and three disks for each endcap; its aim is to contain and to guide the return magnetic field.

3.2 The Tracker

The tracking system is designed to furnish an accurate reconstruction of the flight paths of charged particle emerging from the collisions, together with a precise determination of secondary vertices.

In a proton-proton collision, the momentum of the interacting partons

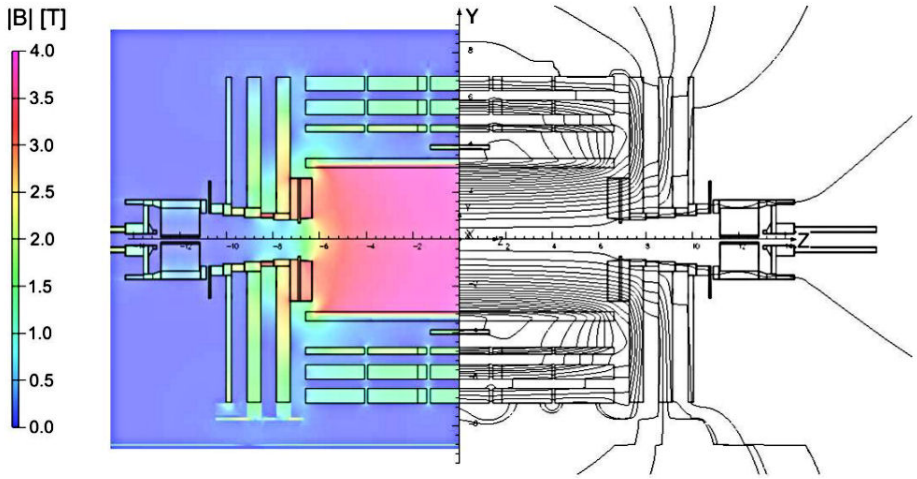

Figure 3.3: The superconducting magnet and the generated magnetic field.

is not exactly known (only on a statistical basis), moreover the longitudinal momentum of the collision products is typically hard to measure, thus the determination of physical observables is usually performed in the transverse plane. For these reasons it becomes essential to measure the transverse momentum $p_T = p \cdot \sin(\theta)$ with high resolution. A particle of charge $Q = z \cdot e$ and transverse momentum p_T that goes through a magnetic field B has an helicoidal trajectory with radius R. The transverse momentum can be expressed by the relation:

$$p_T\,[GeV] = 0.3\ z \cdot B\,[T] \cdot R\,[m]\,. \tag{3.1}$$

Experimentally one measures the curvature $k = Q/R$. In order to take into account the error on the resolution of the measurement and the error due to the multiple scattering of particles, that modifies the trajectories, the error on the curvature can be expressed by the sum in quadrature of the two contributes:

$$\delta k = \sqrt{\delta k^2_{res} + \delta k^2_{MS}}. \tag{3.2}$$

This formula can be parametrized in terms of p_T, the particle transverse momentum resolution, and can be written as:

$$\frac{\delta p_T}{p_T} = C_1 p_T \oplus C_2 \tag{3.3}$$

where C_1 depends on the detector geometry, in particular on the number of points used for the track reconstruction (n), the length of the track (L), and the resolution on the single point measurement (σ_x)

$$C_1 \propto \frac{\sigma_x}{\sqrt{n} \cdot B \cdot L^2} \tag{3.4}$$

while the term C_2 takes into account the multiple Coulomb scattering effects, that dominates for low energy particles.

The coefficient C_1 can be minimized using a long tracker detector, to increase L, having a large number of points n, and minimizing σ_x. The resolution on the single point measurement can be expressed by the sum in quadrature of σ_{int}, the intrinsic resolution of the detectors, and σ_{syst}, the systematic error given by the unknown spatial position of hit module (that can be minimized via alignment procedures):

$$\sigma_x = \sqrt{\sigma_{int}^2 + \sigma_{syst}^2}. \tag{3.5}$$

The tracking system is composed of two systems based on silicon sensor technology, pixel detectors and silicon strip detectors, and its construction necessitated the fulfillment of the following requirements:

- the components must be radiation hard, since the large number of particles created in the collisions exposes the tracking system to a large radiation dose;
- the detectors must have a fast response, since there is a bunch-crossing every 25 ns;
- the need to achieve a high precision in the measurements of the tracks requests fine spatial granularity;
- the amount of material crossed by the particles must be reduced as much as possible for the reason that photon conversion, electron energy loss via Bremsstrahlung and multiple Coulomb scattering of charged particles adversely affects the position resolution of the tracker;
- there must be perfect alignment, internal of its components and with the muon system, in order to provide a reliable measurement of the particle momentum.

The Tracker detector was designed in order to fulfill these requirements, giving at its nominal performance:

- reconstruction capability in the region $|\eta| < 2.54$ with an efficiency of at least 95% for charged tracks with $pT > 10$ GeV;
- high momentum resolution for isolated tracks:

$$\frac{\delta p_T}{p_T} = (1.5 p_T[TeV] \oplus 0.5)\,\% \quad \text{for } |\eta| < 1.6 \tag{3.6}$$

$$\frac{\delta p_T}{p_T} = (6.0 p_T[TeV] \oplus 0.5)\,\% \quad \text{for } |\eta| < 2.5 \tag{3.7}$$

  As is shown in Fig. 3.4, adding the measurements from the muon system, the resolution for $p_T > 0.1$ TeV muons, becomes:

$$\frac{\delta p_T}{p_T} = 4.5\% \cdot \sqrt{p_T} \tag{3.8}$$

- high resolution for both transverse, $\sigma(d_{xy}) = 35$ μm, and longitudinal impact parameter, $\sigma(d_z) = 75$ μm.

Silicon detectors provide a high spatial resolution (from 10 to 20 μm) together with a fast (below 10 ns) collection of the charge deposited by the particles on the sensitive elements. A scheme of the tracking system is shown in Figure 3.5. Three layers of pixel detectors are located at radii of 4.4, 7.3 and 10.2 cm surrounding the beam pipe, and two turbin-like disks are positioned on each side. The silicon strip tracker occupies the radial region between 20 and 116 cm and it's divided in the Tracker Inner Barrel and Disks (TIB/TID), surrounded by the Tracker Outer Barrel (TOB). To extremes, two Tracker EndCaps (TEC+ and TEC -) are located, each one composed by 9 disks, carrying up to 7 rings of silicon micro-strip detectors.

The Pixel Detector The pixel tracker is composed of approximately 66 million pixel cells, with size 100×150 μm^2, that allow a fine 3D vertex reconstruction. Both $r\phi$ and z coordinates are important, and this is why the cells are nearly square-shaped. The pixel detector, both in the barrel and in the endcaps, covers a pseudorapidity range $|\eta| < 2.5$. The layers are composed of modular detector units (called "modules") placed on carbon fiber supports (called "ladders"). Each ladder includes eight modules, consisting of thin (285 μm), segmented silicon sensors with highly integrated readout chips (ROC) connected by Indium bump-bonds. Each ROC serves

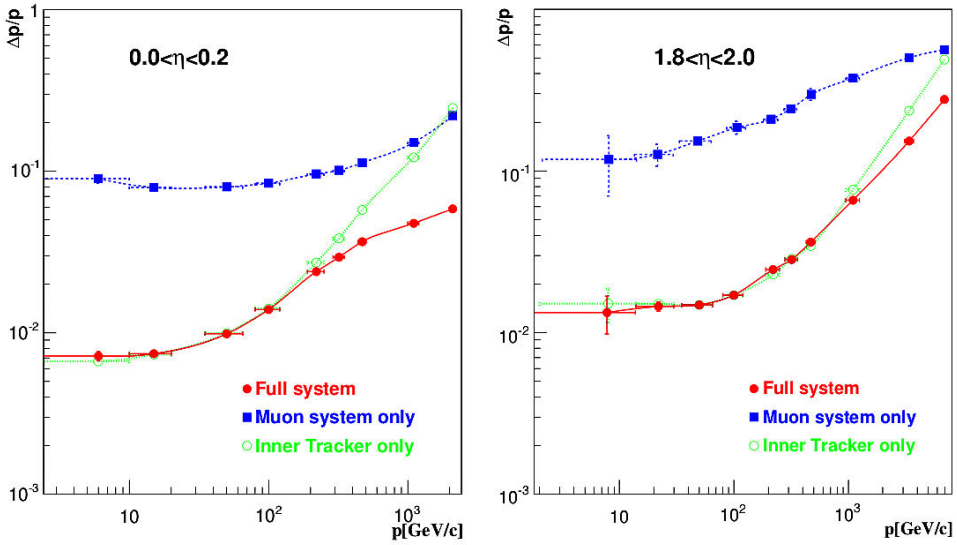

Figure 3.4: Expected momentum resolution of muons as a function of momentum p, using measurements of the muon system only (blue), the tracker only (green) or both detectors (red). Left: central region $0 < |\eta| < 0.2$. Right: forward endcap region $1.8 < |\eta| < 2.0$.

a 521×80 array of pixels. The Barrel Pixel (BPIX) region is composed of 672 full modules and 96 half modules, each including 16 and 8 ROCs, respectively. The number of pixels per module is 66560 (full modules) or 33280 (half modules). The total number of pixels in the barrel section is 47923200. The Forward Pixel (FPIX) endcap disks, extending from 6 cm to 15 cm in radius, are placed at $z = -35.5$ cm and $z = -48.5$ cm. Disks are split into half-disks, each including 12 trapezoidal blades arranged in a turbine-like geometry. Each blade is a sandwich of two back-to-back panels. Rectangular sensors of five sizes are bump-bonded to arrays of ROCs, forming the so-called "plaquettes". Three (four) plaquettes are arranged on the front (back) panels with overlap to provide full coverage for charged particles originating from the interaction point. The endcap disks include 672 plaquettes (270 μm thick), for a total of 17971200 pixels. The minimal pixel cell area is dictated by the readout circuit surface required for each pixel. Since the deposited charge is often shared among several pixels, an analog charge readout is implemented. Charge sharing enables interpolation between pixels, which improves the spatial resolution.

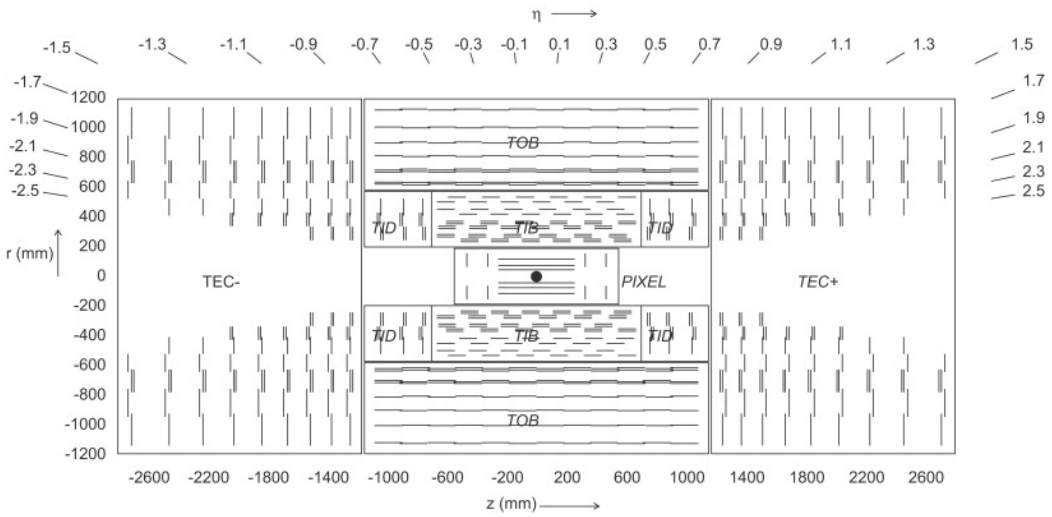

Figure 3.5: Overview of the CMS tracker, where each line represents a detector module.

The Strip Detector The strip tracker is made of 10 layers of silicon microstrip sensors. Various types of sensor geometries are used: rectangular sensor types for TIB and TOB, and wedge-shaped sensor types for TEC and TID. These sensors can be made quite large, so in the innermost barrel their dimension is 6×12 cm^2, and 10×9 cm^2 in the outmost barrel.

The barrel region is divided into the TIB and the TOB. The TIB is composed of 4 layers using silicon sensors with a thickness of 320 μm and a inter-strip distance (strip pitch) which varies from 81 to 118 μm. The TOB is made of 6 layers of thick (550 μm) silicon sensors with a strip pitch which varies from 120 to 180 μm.

The endcaps are diveded into the TEC and the TID. Each TEC is made of 9 disks: the three innermost rings are made of sensors 320 μm thick, while in the remaining disks they are 500 μm thick. The TID comprises 3 disks and the thickness of the sensors is 320 μm. In both trackers, the modules are arranged in rings, their strips point towards the beam line, and they have a variable pitch.

3.3 ECAL: the Electromagnetic Calorimeter

The aim of the electromagnetic calorimeter is the accurate measurement of energy and position of photons and electrons created in the collisions,

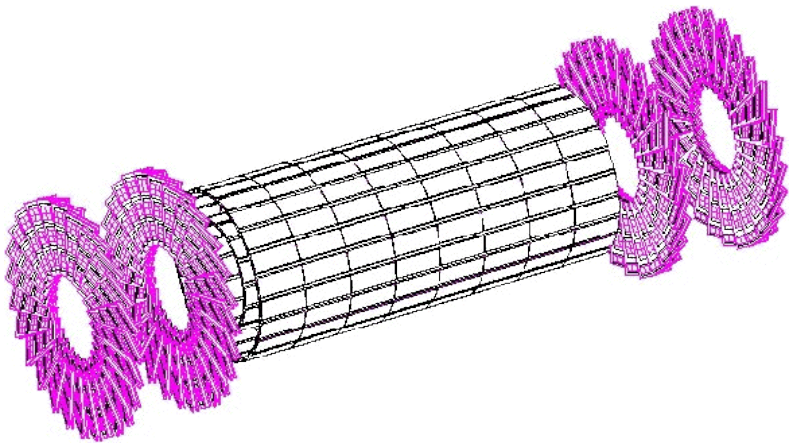

Figure 3.6: Overview of the pixel detector

through their interaction with the material and the collection of the energy released.

The ECAL is a homogeneous calorimeter made of 61200 truncated pyramidal-shaped lead tungstate ($PbWO_4$) crystals mounted in the central barrel part, closed by 7324 crystals in each of the two endcaps. In the barrels, avalanche photodiodes (APDs) collect the light while, in the endcaps, vacuum phototriodes (VPTs) are used.

Like the silicon tracker, the ECAL must be radiation hard and have fine granularity. The high density (8.28 g/cm^3), short radiation length X_0 (0.89 cm) and small Moliére radius (2.2 cm) of lead tungstate crystals permitted the achievement of these targets. The scintillation decay time of $PbWO_4$ is of the same order of magnitude as the bunch-crossing time, indeed about 80% of the light is emitted in 25 ns, and this makes these crystal sufficiently fast for CMS purposes. The homogeneous crystal calorimeter provides a great energy resolution, essential to reconstruct the decay to two photons of a Higgs boson.

A pre-shower device is placed in front of the endcaps. It's made of two disks of lead absorber at $2X_0$ and $3X_0$, and of two planes of silicon strip detectors. It allows the rejection of photon pairs from π^0 decays and improves the estimation of the direction of photons, to enhance the measurement of the two-photon invariant mass.

The barrel covers the pseudorapidity range $0 < |\eta| < 1.479$, while the endcaps cover the interval $1.479 < |\eta| < 3$.

The energy resolution of a module is a function of the energy of the

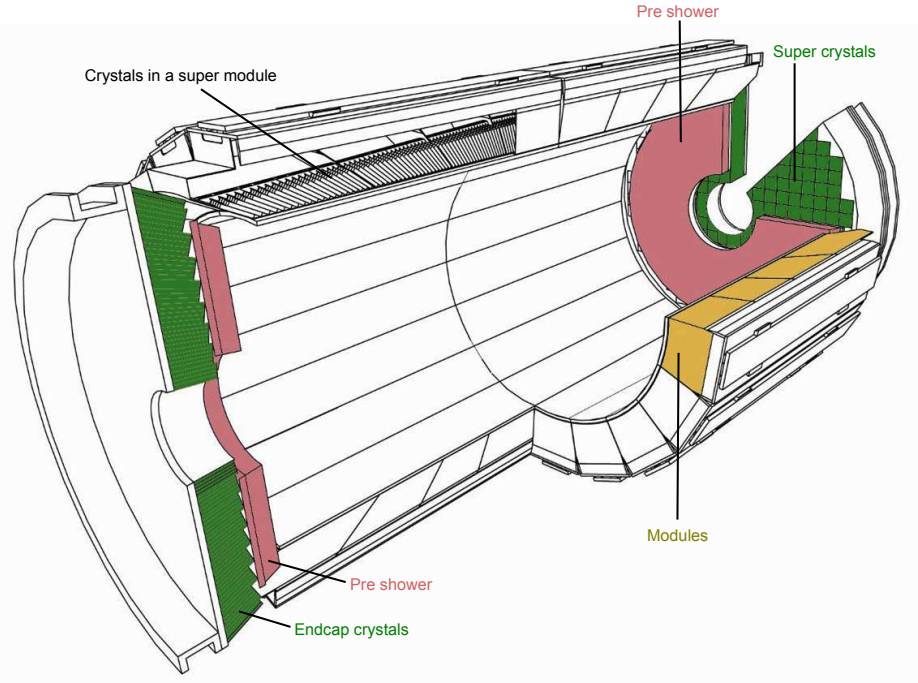

Figure 3.7: Overview of the ECAL.

incident particle, E, and can be parametrized as:

$$\left(\frac{\sigma_E}{E}\right)^2 = \left(\frac{S}{\sqrt{E}}\right)^2 + \left(\frac{N}{E}\right)^2 + C^2 \tag{3.9}$$

where S is the stochastic term that includes the effects of the fluctuations in the number of photo-electrons, N is the noise due to electronics and pile-up and C is a constant term related to the calibration of the calorimeter. The values of the three constants measured on test beams are reported in Table 3.1.

Contribution	Barrel ($\eta = 0$)	Endcaps ($\eta = 2$)
Stochastic term S	2.7%	5.7%
Noise (low luminosity) N	0.155 GeV	0.205 GeV
Noise (high luminosity)	0.210 GeV	0.245 GeV
Constant term C	0.55%	0.55%

Table 3.1: Different contributions to the energy resolution of ECAL.

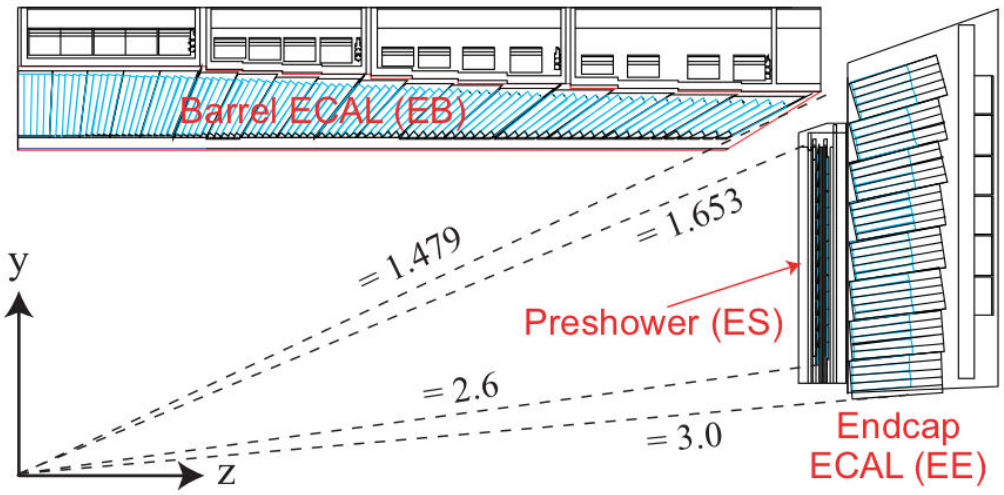

Figure 3.8: Schematic view of the ECAL.

3.4 HCAL: the Hadronic Calorimeter

The design of the HCAL is strongly influenced by its aims: the measurement of energy and direction of hadronic jets, the accurate determination of total transverse energy and of the missing transverse energy of the events. Hence, an important requirement of the HCAL is the high hermeticity (the ability to capture every particle emerging from the collisions) which means that the detector must cover a portion of the solid angle as big as possible. For this reason, the barrel and endcaps are complemented by a very forward calorimeter which is placed outside the magnet return yokes, with a total coverage of $|\eta| < 5.31$. The barrel and endcaps cover the region $|\eta| < 3.0$. They are sampling calorimeters, whose active elements are plastic scintillators interleaved with brass absorber plates and read out by wavelength-shifting fibres. The first layer is read out separately, while all others are read out together. Brass has been chosen as absorber material for its short interaction length, and is non-magnetic. The photodetection readout is based on multi-channel hybrid photodiodes (HPDs) that can operate in a high magnetic field and give an amplified response, proportional to the original signal, for a large range of particle energies. The HPDs are housed within the calorimeter volume. In the barrel, full shower containment is not possible within the magnet volume, and an additional tail catcher is placed outside the magnet consisting of an additional layer of scintillators. The very forward calorime-

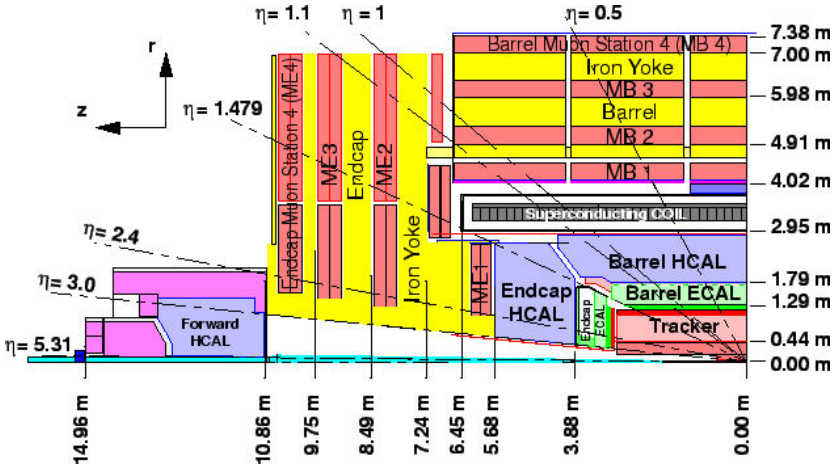

Figure 3.9: Schematic view of the detector that shows the different η coverage of the various parts of the HCAL.

ter is placed outside the magnet yoke, 11 m from the interaction point. The active elements are quartz fibres parallel to the beam, inserted in steel absorber plates. The signal originated from quartz fibres is Čerenkov light. The expected energy resolution (E in GeV) is $\sigma/E \simeq 65\%\sqrt{E} \oplus 5\%$ in the barrel, $\sigma/E \simeq 85\%\sqrt{E} \oplus 5\%$ in the endcaps and $\sigma/E \simeq 100\%\sqrt{E} \oplus 5\%$ in the very forward calorimeter.

3.5 The Muon System

The efficient detection of muons is of primary importance, as they represent a clear signature for a large number of physical processes. The muon system fulfills three purposes: muon identification, momentum measurement, and triggering. As stated previously, the return yoke hosts the muon system, thanks to which the detectors are shielded from charged particles other than muons.

The produced muons are measured not only in the muon system but also in the inner tracker. The measurement of the momentum of muons, using only the muon system, is performed through the determination of the muon bending angle at the exit of the coil, taking the interaction point (known with a precision of ≈ 20 μm) as the origin of muons. The resolution of this measurement is labelled as "Muon system only"in Figure 3.4. For p_T up to 200 GeV, the resolution is dominated by multiple scattering; above this value

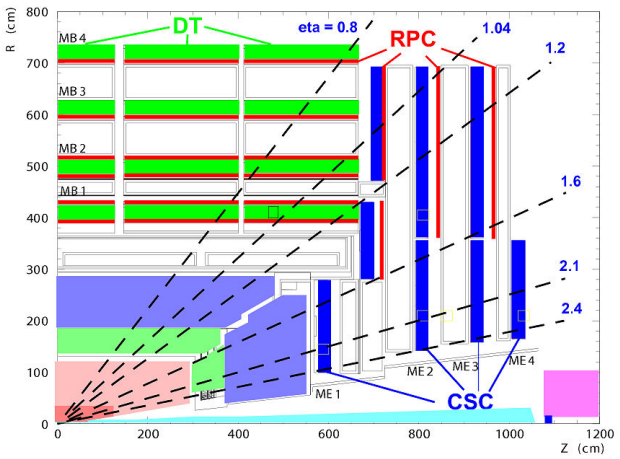

Figure 3.10: Layout of a quarter of the muon system.

of the transverse momentum, the chamber spatial resolution dominates. For low-momentum muons, the best resolution is that obtained in the silicon tracker; in Figure 3.4 it is labelled as "Inner Tracker only". The minimum energy required to reach the muon system is about 5 GeV.

To identify and measure muons, three types of subdetectors are used. In the barrel ($|\eta| < 1.2$), where the muon rate and the residual magnetic field are low, four layers (stations) of drift tube chambers (DT) are used. The chamber segmentation follows that of the iron yoke, consisting of 5 wheels along the z axis, each one divided into 12 azimuthal sectors. Each chamber has a resolution of ≈ 100 μm in $r\phi$ and 1 mrad in ϕ.

In the two endcaps ($0.8 < |\eta| < 2.4$), where the muon rate and the residual magnetic field are higher, cathode strip chambers (CSC) are used. In each of the endcaps, the chambers are arranged in 4 disks perpendicular to the beam, and in concentric rings (3 rings in the innermost station, 2 in the others). Each chamber has a spatial resolution of about 200 μm (100 μm for the first station of chambers) and an angular resolution of about 10 mrad. In both the barrel and the endcaps, a system of resistive plate chambers (RPC) is installed to assure redundancy to the measurement. RPCs provide a rougher spatial resolution than DTs and CSCs, nevertheless they provide a fast response with a good time resolution.

3.6 Trigger System and Data Acquisition

At present time, no storage system is capable of acquiring the large amount of data produced at LHC due to the high interaction rate. Since the typical size of a raw event is ≈ 1 MB, only a rate of ≈ 100 Hz can be stored, while the collision rate is 40 Hz ($\approx 10^9$ interactions/sec) at design luminosity; thus, a huge rejection factor is needed. The trigger system must be capable to reduce the rate while maintaining a high efficiency on the (potentially) interesting events.

The trigger and the data acquisition systems consist of 4 parts: the detector electronics, the Level-1 trigger processors (calorimeter, muon, and global), the readout network, and the online event filter system that executes the software for the High-Level Triggers (HLT).

3.6.1 The Level-1 Trigger

The Level-1 Trigger restricts the rate of the selected events down to 50 kHz (which corresponds to a design output rate limit of 100 kHz). The limits due to the physical dimensions of the detectors and the caverns, impose a minimum time for the signals to reach the cavern that hosts the Level-1 trigger logic and to go back to the detector front-end electronics. For this reason, the time needed for reaching the decision to keep or discard the data from a certain event is 3.2 μs. While waiting for the decision, the high-resolution data is pipelined in order to reduce the deadtime.

The L-1 trigger involves the calorimetric measurements and the muon system. The trigger decision is based on the so called "trigger primitive", that is the presence of objects like electrons, photons, muons, and jets with a E_T or a p_T above the threshold. The structure of the L-1 trigger is illustrated in Figure 3.11. The Calorimeter Trigger finds the best electrons, photons, and jets candidates; moreover, it determines the total transverse energy, the missing energy and the scalar transverse energy sum of all jets above a programmable threshold.

For what concerns the Muon Trigger, all the three trigger systems – RPCs, CSCs, and DTs – take part in the trigger: the CSC and DT track finders join the segments to complete the tracks and to assign physical values to them, while the RPC trigger chambers, thanks to their high timing resolution, deliver their own track candidates. The muon candidates are then passed to the Global Muon Trigger, which combines the informations from the various sub-detectors to improve the momentum resolution and the ef-

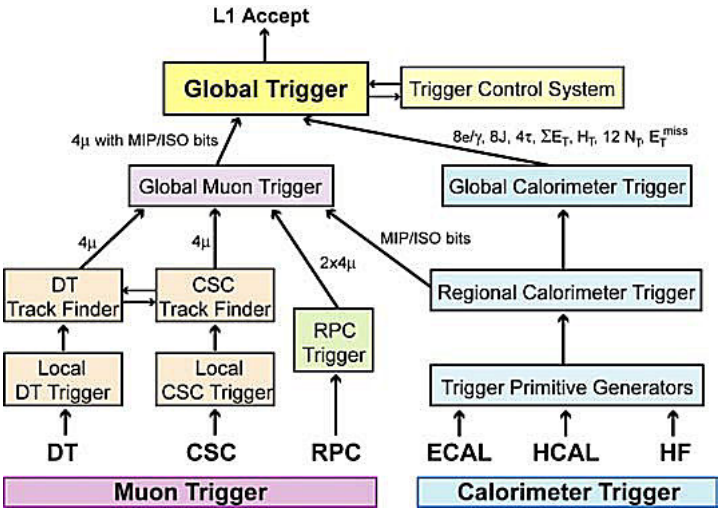

Figure 3.11: Model of the L-1 trigger.

ficiency with respect to the individual systems. Finally, the Global Trigger decides to accept or reject the event at the Level-1 Trigger.

3.6.2 The High Level Trigger (HLT)

Right after the Level-1 Trigger, the data from a given event are transferred to a processor. There are about a thousand of processors, each performing the same HLT software code, and they have to reduce the output rate from 100 kHz to about 100 Hz to allow the storage. The HLT doesn't reconstruct all the objects in an event, but only the actually needed ones, in order to reject the uninteresting objects as soon as possible. This can be done thanks to three level triggers: initially, only the informations from the calorimeters and the muon systems are used, then the informations from the silicon tracker are added, and finally the full available event information is exploited.

3.6.3 The Data Acquisition (DAQ)

The scheme of the CMS DAQ system is shown in Figure 3.12. Like the HLT, the crucial function of the DAQ system is to read the CMS detector information for the events selected by the Level-1 Trigger, and to select the most interesting ones for output to mass storage. Thus, it must sustain a data flow of $\approx$ 100 GB/s ($\approx$ 1 MB/evt) coming from $\approx$ 650 data sources, each with an average event fragment size of $\approx$ 2 kB (for pp collisions at the

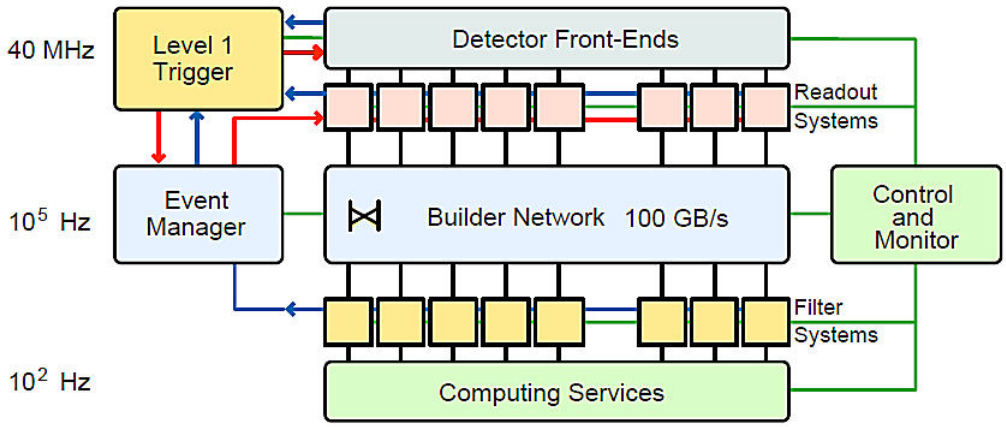

Figure 3.12: Scheme of the Data Acquisition system.

design luminosity 10^{34} cm^{-2}s^{-1}), and must provide enough computing power for the HLT to reduce the rate of stored events from 100 kHz to 100 Hz.

All events that pass the Level-1 Trigger are sent to the Event Filter that performs physics selections to filter events and achieve the required output rate. Each sub-detector has a front-end system (FES) that stores data in pipelined buffers. There are approximately 700 FESs in the CMS readout. When a L-1 trigger arrives, the Timing-Trigger-Control (TTC) system pulls out the corresponding data from the front-end buffers and pushes them into the DAQ system via the Front-End Drivers (FEDs). Here the Front-end Read-out Links (FRLs) read the data. The event builder assembles the event fragments belonging to the same L-1 from all FEDs into a complete event and transmits it to one Filter Unit (FU) in the Event Filter for further processing. The collection of networks that provide the interconnections between the Read-out and the Filter Systems is known as Builder Network. The DAQ system can be deployed in up to 8 nearly autonomous systems, each capable of handling up to 12.5 kHz event rate.

3.6.4 Software and Computing

The CMS software and computing systems need to store, reconstruct and analyze such an amount of data that exceeds the capabilities of CERN's central computing systems. Therefore, the CMS computing system is distributed worldwide, with a primary "Tier-0"centre placed at CERN, com-

plemented by "Tier-1" and "Tier-2" located at large national laboratories or research institutes in CMS collaborating countries (*e.g.* INFN in Italy). The T-0 has to accept, archive and distribute RAW data collected from the CMS Online Data Acquisition and Trigger System (TriDAS), to perform prompt calibration in order to get the calibration constants needed to run the reconstruction, to perform prompt first reconstruction which produces the RECO dataset, and to transfer the prompt reconstructed RECO and RAW datasets to the T-1. The T-1 is a set of seven sites with the task of archive and redistribute to T-2 the RAW, RECO, AOD and Monte Carlo samples. The T-2 is a numerous set of small sites, each with considerable CPU resources. It provides capacity for user analysis, calibration studies, and Monte Carlo production. It provides limited disk space, and no tape archiving. T-2 centers rely upon T-1s for access to large datasets and for secure storage of the new data (*i.e.* Monte Carlo simulations) produced at the T-2. CMS data are

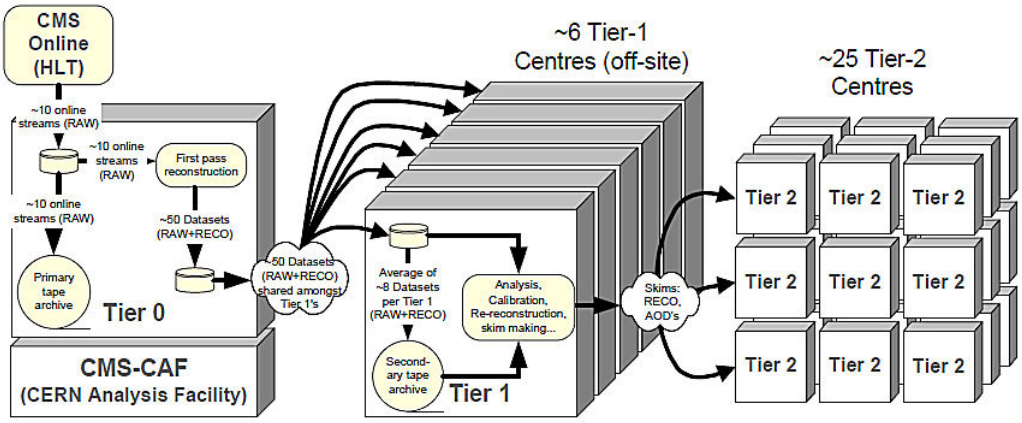

Figure 3.13: Dataflow between the various CMS computing systems.

arranged into different level of detail and precision. The main data formats are:

- RAW: they contain all the recorded informations from the detector together with other data like the trigger decision. They are permanently archived in safe storages, where they occupy approximately 1.5 – 2 MB/evt, but they aren't directly used for analysis purposes;
- RECO: these are the reconstructed data, obtained from the RAW data in several steps:

  - detector-specific filtering and correction of the digitized data: detector calibration constants are applied to reconstruct the objects;
  - cluster- and track-finding: it involves the hits in the silicon tracker and the muon detectors to reconstruct the global tracks;
  - primary and secondary vertex reconstruction;
  - particle ID: reconstructs standard physical objects like electrons, photons, muons and so on using a variety of complicated algorithms;

- AOD: they are produced filtering RECO data, thus obtaining a compact analysis format which contains the various parameters of the physical objects and additional informations to allow kinematical refitting. They are a good compromise between information complexity and size, since this format requires approximately 100 kB/evt.

The overall collection of software is referred as CMSSW and it's built around a Framework, an Event Data Model (EDM) and Services needed by all the event processing (*e.g.* simulation, calibration, aligment, reconstruction). The main aim of the Framework and the EDM is to facilitate the development and deployment of reconstruction and analysis software. The EDM is centered around the "Event"object, which contains all data representing the raw detector output, and the reconstruction and simulation products, together with "metadata"describing the configuration of the software used for the reconstruction of the data objects and the conditions and the calibration data used for such reconstructions. All objects in the Event may be stored in ROOT files, thus directly browsable in ROOT. The CMS executable (`cmsRun`) is configured at run time by a collection of parameter/-value pairs created from a user-written configuration file. This configuration file tells cmsRun which data to use, which modules to execute and in which order (path), which is the parameter setting to use with each module, how the events are filtered within each path and how the paths are connected to the output files. Because of the large amount of data involved, a fully distributed computing model is used for data reconstruction and analysis. The system is based upon Grid middleware, with the common Grid services at centres defined and managed through the Worldwide LHC Computing Grid (WLCG) project, a collaboration between LHC experiments, computing centres, and middleware providers.

Chapter 4

Data Analysis

The goal of this analysis is the evaluation of the fraction of the $\Upsilon(3S)$ originating from the $\chi_b(3P)$ decays, that is the "feed-down"contribution, obtained by the ratio

$$\frac{\sigma\left(\chi_b(3P) \to \Upsilon(3S)\gamma\right)}{\sigma\left(\Upsilon^{inc}(3S)\right)} \tag{4.1}$$

that is

$$\frac{\sum\limits_{J=0,1,2} \sigma\left(pp \to \chi_{bJ}(3P)X\right) \cdot \mathcal{B}\left(\chi_{bJ}(3P) \to \Upsilon(3S)\gamma\right)}{\sigma\left(pp \to \Upsilon(3S)X\right) + \sum\limits_{J=0,1,2} \sigma\left(pp \to \chi_{bJ}(3P)X\right) \cdot \mathcal{B}\left(\chi_{bJ}(3P) \to \Upsilon(3S)\gamma\right)} \tag{4.2}$$

The numerator, $\sigma\left(\chi_b(3P) \to \Upsilon(3S)\gamma\right)$, represents the production cross section in pp collisions for the $\chi_b(3P)$, $\sigma\left(pp \to \chi_b(3P)X\right)$, times the branching ratio in the decay channel of interest, $\mathcal{B}\left(\chi_{bJ}(3P) \to \Upsilon(3S)\gamma\right)$, and the denominator, $\sigma\left(\Upsilon^{inc}(3S)\right)$, is the cross section for the inclusive production of the $\Upsilon(3S)$ meson, given by the sum of the directly produced $\Upsilon(3S)$, $\sigma(pp \to \Upsilon(3S)X)$, and those resulting from $\chi_b(3P)$ radiative decay, $\sigma\left(pp \to \chi_{bJ}(3P)X\right)$ $\cdot\mathcal{B}\left(\chi_{bJ}(3P) \to \Upsilon(3S)\gamma\right)$. The sum over J takes into account the contribution to the cross sections of each χ_{bJ} state, while X refers to any final state.

Actually, this work considers only $J = 1$ and $J = 2$ spin states for the $\chi_b(3P)$, while the $J = 0$ is not considered due to its very low expected[1] branching ratio in the radiative decay $\Upsilon + \gamma$ with respect to the other spin states, thus a negligible contribution is expected.

The results presented here use a data sample collected at the LHC with the CMS detector at a centre-of-mass energy of 8 TeV and corresponds to

[1] in analogy with $\chi_c(1P)$ and $\chi_b(nP)$, $n = 1, 2$ measurements.

approximately the 90% of the integrated luminosity collected in 2012, which is shown in Figure 4.1.

At the time of the writing there is no public experimental result for this measurement.

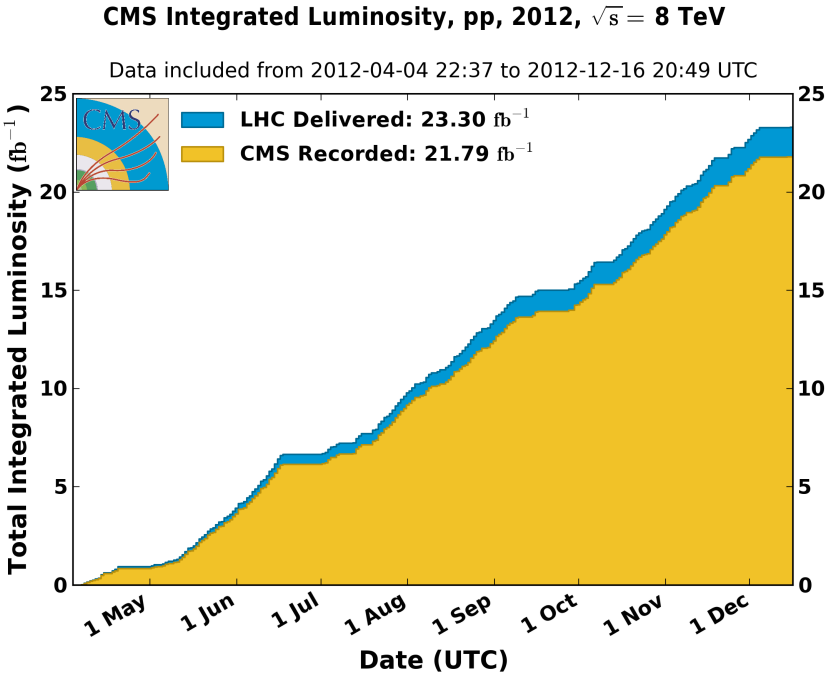

Figure 4.1: Total integrated luminosity vs. time recorded by LHC and CMS during 2012 at a centre-of-mass energy of 8 TeV.

4.1 Experimental Method

To estimate the ratio in Eq.4.2, basically one has to count the number of $\chi_b(3P)$ that decay in $\Upsilon(3S)$, the $\Upsilon^{inc}(3S)$ in the sample and to correct for the efficiency as follows:

$$\frac{\sigma\left(\chi_b(3P) \to \Upsilon(3S) + \gamma\right)}{\sigma\left(\Upsilon^{inc}(3S)\right)} = \frac{N\left(\chi_b(3P) \to \Upsilon(3S) + \gamma\right)}{N\left(\Upsilon^{inc}(3S)\right)} \frac{\varepsilon_{\mu\mu}}{\varepsilon_{\mu\mu} \cdot \varepsilon_{\gamma}} \quad (4.3)$$

$$\approx \frac{N\left(\chi_b(3P) \to \Upsilon(3S) + \gamma\right)}{N\left(\Upsilon^{inc}(3S)\right)} \frac{1}{\varepsilon_{\gamma}} \quad (4.4)$$

The two dimuon reconstruction efficiencies are not precisely equal in principle, as directly produced Υ and those originating from χ_b decay generate muons with different p_T distribution in the two cases, affecting the acceptance, and thus the reconstruction efficiency; to a first approximation they can be assumed as equal, so they cancel out in the ratio. The χ_b mesons are reconstructed through the decay chain $\chi_b(3P) \to \Upsilon(3S) + \gamma$ and $\Upsilon(3S) \to \mu^+ + \mu^-$.

The ECAL has a high efficiency but a rather poor resolution for low-energy photons, while the silicon tracker has good energy resolution($\approx$ 5–15 MeV) and spatial resolution but low efficiency in reconstructing the tracks left by the electron-positron pair inside the silicon tracker. The high spatial resolution of the silicon tracker permits to associate the dimuon vertex with the direction of the photon; on the contrary, this is not possible in the ECAL, which is subject to high pile-up, where this would lead to high background. These reasons lead to choose for this analysis the photon reconstruction through the e^+e^- conversions in the tracker.

For each χ_b candidate, the mass difference $\Delta m = m_{\mu\mu\gamma} - m_{\mu\mu}$ (Q value) between the dimuon-plus-photon invariant mass ($m_{\mu\mu\gamma}$) and the dimuon invariant mass ($m_{\mu\mu}$) is evaluated. The use of the mass difference eliminates the uncertainty due to the finite mass resolution of the dimuon pair, without the need to constrain the mass of the $\mu^+\mu^-$ pair to the mass of the Υ. For plotting the χ_b invariant mass distribution, the quantity $m_{\Upsilon,PDG}$, that is the world-average mass of the Υ from [1], is added to the mass difference.

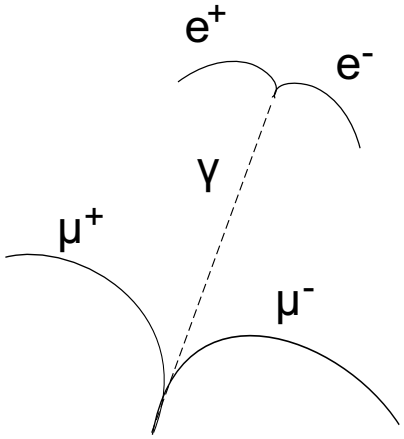

Figure 4.2: Scheme of the decay process considered for this analysis.

4.2 Event reconstruction and selection

4.2.1 $\Upsilon(3S)$ Reconstruction

The Υ mesons are reconstructed identifying the two muons originating from the leptonic decay $\Upsilon \rightarrow \mu^+\mu^-$. The CMS offline reconstruction process distinguishes between three kinds of reconstructed muons:

- standalone muons: only the signal of the muon system (Drift Tubes, Cathode Strip Chambers) are used for the reconstruction;
- tracker muons: only the tracker signal is used for the momentum measurements, while the muon system is used only for identification;
- global muons: uses both silicon and muon chamber informations to reconstruct the muon tracks. In this way it provides a high-quality and high-purity muon reconstruction for tracks with $p_T > 4$ GeV in the central η region, and with $p_T > 1$ GeV in the forward region, but tracker muons reach a better reconstruction efficiency at lower momenta.

For this analysis, the tracker muons are used to reconstruct the momentum. They must satisfy a series of requirements, *i.e.* to have at least 10 hits in the silicon tracker (at least two in the pixel layers) and a compatible signal in the muon chambers. They must have a track fit $\chi^2/n_{d.o.f.}$ smaller than 1.8, and be inside a cylinder of radius 3 cm and length 15 cm, whose barycenter is at (0, 0, 0) with respect to CMS coordinates coaxial with the beam line, in order to reject "fakes"due to cosmic-ray muons and to decays in flight.

Each muon track must have a transverse momentum p_T higher than 3.3 GeV for $|\eta| \leq 1.3$, $p > 2.9$ GeV for $1.3 < |\eta| \leq 2.2$ and $p_T > 0.8$ GeV for $2.2 < |\eta| \leq 2.4$. Events are rejected if the distance in the plane transverse to the beam line between the dimuon vertex and the interaction point is larger than 100 μm (see Figure 4.3), in order to reject muon pairs with an invariant mass in the Υ mass region but which are not dimuons from Υ decays. If more than one dimuon candidate is found in an event, only the one with largest vertex χ^2 probability is retained, anyway this is a rare eventuality.

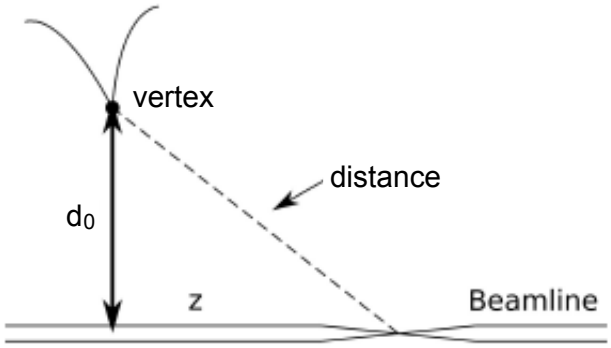

Figure 4.3: Scheme of the dimuon vertex.

4.2.2 γ Reconstruction for $\chi_{b1,2}(3P)$ Candidate Selection

The χ_b candidate reconstruction requires the reconstruction of the photon originating from the radiative decay. The algorithm that performs this reconstruction has been developed by the CMS collaboration and it's described in detail in [9]. The Q value for the radiative decay under examination is around 200 MeV so the emitted photon is relatively soft (*e.g.* with respect to the photons resulting from the Higgs decay $H \to \gamma\gamma$); as a consequence, the e^+e^- are soft, too; furthermore, the energy distribution between the two leptons is usually asymmetric, causing one lepton to have much less energy than the other. The trajectories of these soft particles are bent by the magnetic field becoming three-dimensional helixes, so they are often fully stopped in the silicon tracker and they don't reach the ECAL. Thus, the algorithm that reconstructs these conversions uses only the hits on the silicon tracker, efficiently reconstructing low-p_T and displaced tracks utilizing the iterative tracking described in [9].

The opposite-sign pairs used to find the photon candidate have to fulfill the following requirements: the invariant mass of the pair must be consistent with zero, and the two tracks must be parallel at the conversion vertex and open only in the transverse plane because of the magnetic field. They must have more than 6 hits in the tracker and $\chi^2/n_{d.o.f.} < 10$. Then the conversion pair signature is employed to distinguish between genuine and fake pairs. The primary vertex has to lie outside the track trajectory helix, and the distance of minimum approach in the xy plane, d_{xy}, has to be between

$-0.25\ cm$ and $1\ cm^2$. Further requirements include a small z separation ($|\Delta z| < 5\ cm$) between the tracks innermost points if they are in the barrel and a small opening angle in the longitudinal plane ($\Delta \cot\theta < 0.1$). The two candidate conversion tracks must have one of the innermost two hits in the same detector layer, in order to reduce the contribution of fake conversions due to soft displaced tracks that are artificially backward propagated. Each conversion track candidate must be compatible in z within 5σ with at least one reconstructed primary vertex, and the primary vertex closest in z to each track must be one of the two closest primary vertices of the other track. Track pairs that survive the selection are then fitted to a common 3D-constrained kinematic vertex fitter. The three-dimensional constraint imposes the tracks to be parallel in both transverse and longitudinal planes. The pair is retained only if the fit converges and its χ^2 probability is greater than 5×10^{-4}.

For the analysis under consideration, only reconstructed photons with a conversion radius (vertex transverse distance with respect to the nominal beam spot) larger than $1.5\ cm$ are retained, allowing the suppression of the background contribution due to $\pi^0 \to e^+e^-\gamma$ (Dalitz decay) while retaining photon conversions possibly occurring within the beam pipe volume.

The reconstructed photon is associated to a vertex extrapolating the photon momentum and finding the closest vertex. This vertex is required to be compatible with the reconstructed Υ one by asking their distance to be compatible within five standard deviations; furthermore, none of the two candidate muon tracks building the Υ vertex up must be the candidate electron or positron track of the reconstructed conversion vertex. Finally each conversion candidate is associated to every other conversion candidate in the event, and to any Particle-Flow reconstructed photon. Particle-Flow photons are photons identified with the Particle-Flow algorithm. The Particle-Flow algorithm consist in combining the information of the inner tracker, the electromagnetic and hadron calorimeter to try and associate to every track a cluster in the calorimeters. Once this step has been performed the ECAL clusters that weren't associated to any track are classified as Particle-Flow photons. This kind of photon identification is rather loose allowing a high rate of fake photons. Any conversion building up a pair which invariant mass differs from the PDG π^0 mass less than 25 MeV is rejected, since it is assumed to be compatible with a π^0 decay photon. Finally only reconstructed

[2] $d_{xy} = d_{O_1-O_2} - (R_1 - R_2)$, that is the distance between the two centers of the track circles in the transverse plane, $d_{O_1-O_2}$, and the difference between the two circles radii R_1 and R_2.

photons with $p_T > 0.5$ GeV are retained. In Figure 4.4 distribution of the conversion vertices the hits of the conversion pairs in the tracker are shown.

4.3 Photon Reconstruction Efficiency

As stated in 4.1, the correct estimation of the efficiency in the reconstruction of the photon is of fundamental importance since it defines the success of the χ_b candidates reconstruction. It is clear that there's no way to know exactly the number of $\chi_b(3P)$ produced in the collision. For this reason it becomes essential to resort to Monte Carlo simulations, in order to produce a large number of $\chi_b(3P)$ mesons, simulate their propagation in the subdetectors and finally reconstruct them with the same reconstruction software used for real data.

The photon reconstruction efficiency is thus obtained as follows:

$$\varepsilon_\gamma = \frac{N_{rec}\left(\chi_b(3P) \to \Upsilon(3S)\gamma\right)}{N_{gen}\left(\chi_b(3P) \to \Upsilon(3S)\gamma\right)} \cdot \frac{1}{\varepsilon_{\mu\mu}} \tag{4.5}$$

where N_{rec} are the correctly reconstructed $\chi_b(3P)$, while N_{gen} are the generated ones in the same acceptance region $|y_\Upsilon| < 1.0$, $p_{T,\gamma} > 0.5$ GeV and $p_{T,\Upsilon} > 9.5$ GeV. The ratio N_{rec}/N_{gen} gives the efficiency for the reconstruction of the photon, ε_γ, times the efficiency for the reconstruction of the dimuon pair, $\varepsilon_{\mu\mu}$, thus it is necessary to divide by $\varepsilon_{\mu\mu}$ in order to obtain ε_γ. The dimuon reconstruction efficiency is obtained as follows:

$$\varepsilon_{\mu\mu} = \varepsilon_{\mu 1} \cdot \varepsilon_{\mu 2} \cdot \rho \tag{4.6}$$

where $\varepsilon_{\mu 1}$ and $\varepsilon_{\mu 2}$ are the single muon efficiencies and ρ allows for the dimuon correlation introduced by the detectors. The ρ factor is sufficiently close to 1 that its influence can be discarded. For each event, a muon identification efficiency is coupled with the p_T of each of the two muons originating from the $\Upsilon(3S)$. The values of the single muon efficiencies are taken from the Analysis Note [11] and are shown in Figure 4.5. The average over the sample of the product of the two efficiencies gives $\varepsilon_{\mu\mu} = (0.88 \pm 0.01)$, where a 1% error has been associated to the single muon efficiency.

4.3.1 Monte Carlo simulations configuration

For this analysis, a PYTHIA6-based particle gun has been used. The particle gun generates single χ_b particles, bypassing the problems due to the low

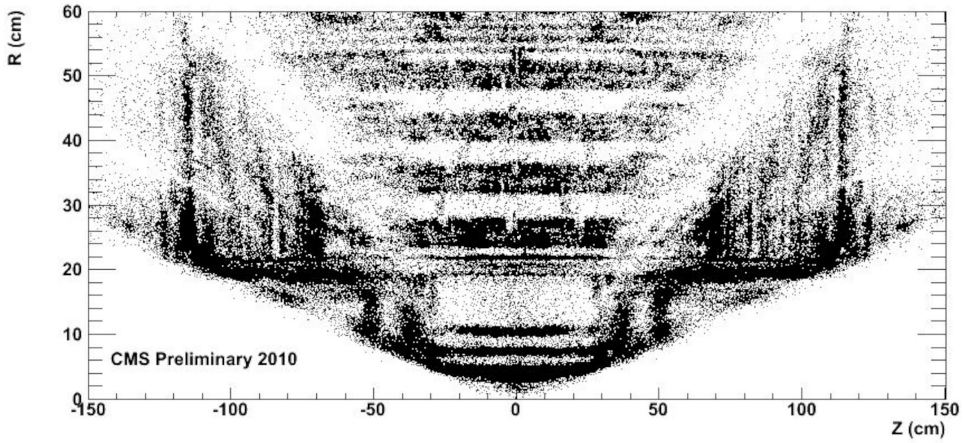

(a)

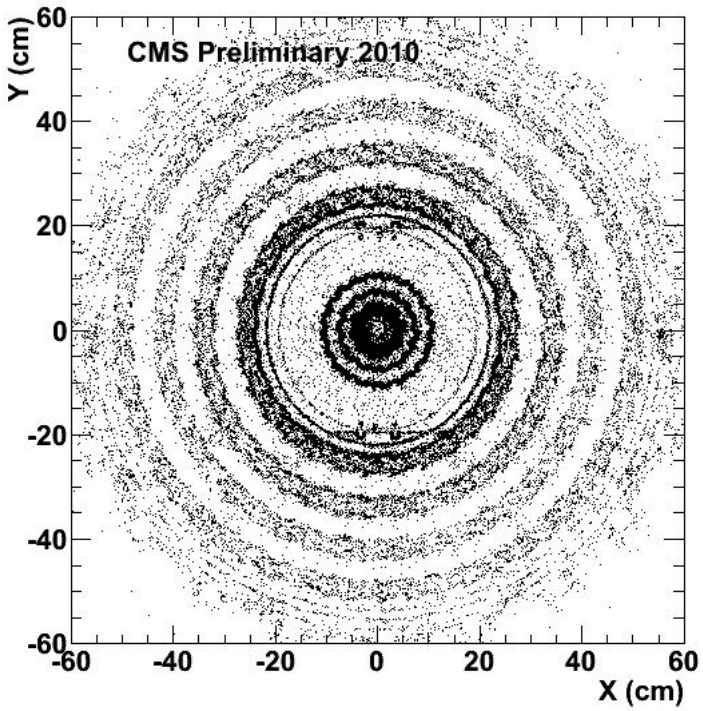

(b)

Figure 4.4: Conversion vertices in the zR (a) and in the xy plane for $|z| < 26$ cm (b).

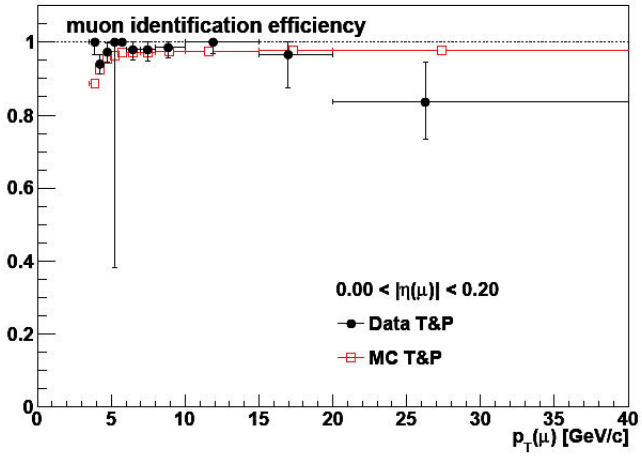

Figure 4.5: Muon reconstruction efficiency vs. p_T for the pseudorapidity range $|\eta_\mu| < 0.2$.

photon reconstruction efficiency. The produced χ_b and all its decay products are then propagated in the detector and are finally reconstructed through their interactions with the subdetectors. Only $\chi_b(3P)$ states are generated, with $J = 1$ in 57% of the events and with $J = 2$ in the remaining 43% of the events, while the contribution of $J = 0$ spin state is neglected. The ratio between the spin states has been chosen by analogy with the well known χ_c case [10], since these quantities are unknown for χ_b mesons.

PYTHIA creates χ_b mesons that are forced to decay in $\Upsilon + \gamma$, and all the Υ mesons are forced to decay into a $\mu^+\mu^-$ pair. Here is the significant part of the code:

```
'MSEL=61                    ! Quarkonia',
'MDME(1035,1)=1             ! Upsilon -> mumu turned ON',
'BRAT(1565)=1.0             ! chi_1b->Upsilon gamma',
'BRAT(1043)=1.0             ! chi_2b->Upsilon gamma',
```

PYTHIA doesn't describe (3P) states, so it is necessary to use some tricks: the decay chain $\chi_{b1,2}(1P) \to \Upsilon(1S) + \gamma$ is generated, then the masses for 1P/1S states are substituted with 3P/3S masses. While the mass of the $\Upsilon(3S)$ is chosen according to the value reported in the Particle Data Group [1], there is not any experimental measurement for the mass splitting between $\chi_{b1}(3P)$ and $\chi_{b2}(3P)$ masses, thus theoretical predictions [12] have been used. Here are the few lines that have been added to the code to force

PYTHIA to describe the decay of interest:

```
'PMAS(294,1)=10.524        ! Mass of chi_b1(3P) ',
'PMAS(148,1)=10.539        ! Mass of chi_b2(3P) ',
'PMAS(147,1)=10.3552       ! Mass of Upsilon(3S) ',
```

One of the parameters passed along the particle gun is the p_T distribution of generated $\chi_b(3P)$. The lack of works about the transverse momentum at generation of these mesons at LHC makes some approximations necessary. Since the $\Upsilon(3S)$ is the closest particle (in mass and other properties), its p_T, of which the distribution has been studied in [13], is used. In the work [13], fitting the p_T spectrum of the $\Upsilon(3S)$, the parametrization below is extracted:

$$f(x) = a \cdot x \cdot b^{\frac{1+x^2}{c}} \tag{4.7}$$

where the parameters have the following values:

$$\begin{aligned} a &= \quad 0.10 \\ b &= \quad 3.05 \\ c &= 84.50 \end{aligned}$$

The plot of the p_T distribution of the $\Upsilon(3S)$ used for the $\chi_b(3P)$ is shown in Figure 4.6.

The $\chi_b(3P)$ are generated only in the kinematical region 5 $GeV < p_T <$ 40 GeV in the whole range of ϕ values, and within 2 units of pseudorapidity, as is shown in the fragment of code below:

```
MinPhi = cms.double(-3.14159265359),
MaxPhi = cms.double(3.14159265359),
MinPt  = cms.double(5.0),
MaxPt  = cms.double(40.0),
MinEta = cms.double(-2.0),
MaxEta = cms.double(2.0),
```

4.3.2 Results

The data obtained from the Monte Carlo are analyzed applying the same selection cuts for both the generated and the reconstructed particles, that is $|y_\Upsilon| < 1.0$, $p_{T,\gamma} > 0.5$ GeV and $p_{T,\Upsilon} > 9.5$ GeV. With these cuts, 497 reconstructed χ_b and 1466450 generated χ_b are selected.

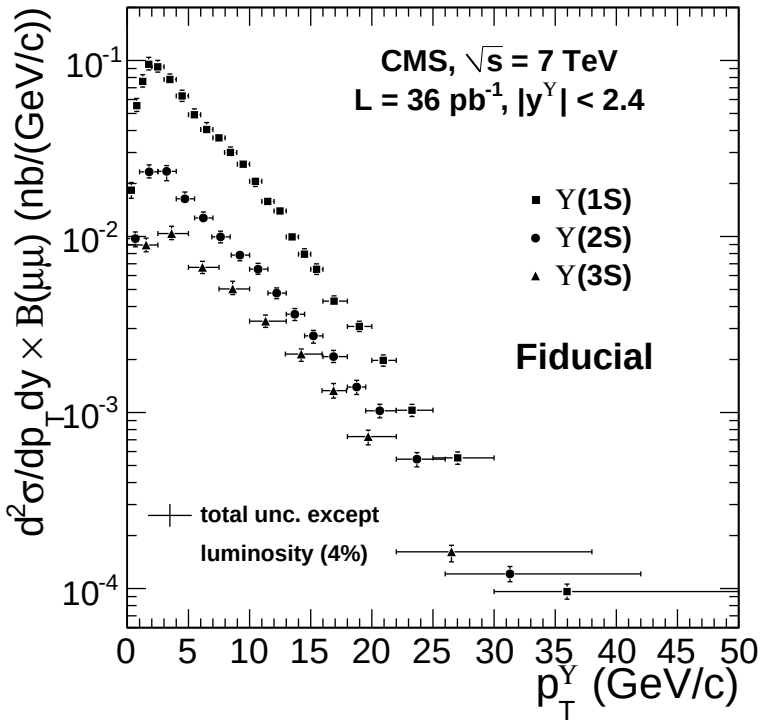

Figure 4.6: Differential fiducial cross sections of the $\Upsilon(nS)$ as a function of p_T in the rapidity range $|y| < 2.4$ [13].

In Fig. 4.7, the invariant mass distributions for the $\Upsilon(3S)$ and the $\chi_b(3P)$ from the reconstructed events of the particle gun are shown.

Using the Eq. 4.5, the efficiency is calculated to be:

$$\varepsilon_\gamma = (3.85 \pm 0.18) \cdot 10^{-4} \tag{4.8}$$

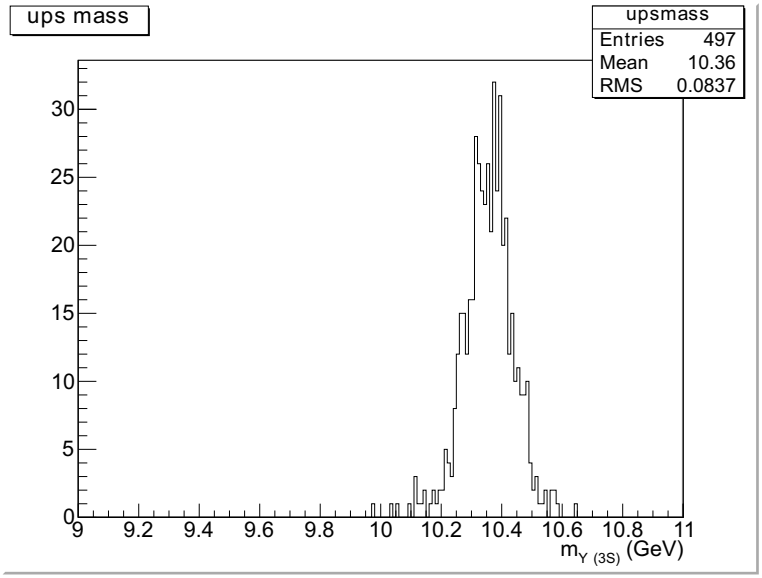

(a)

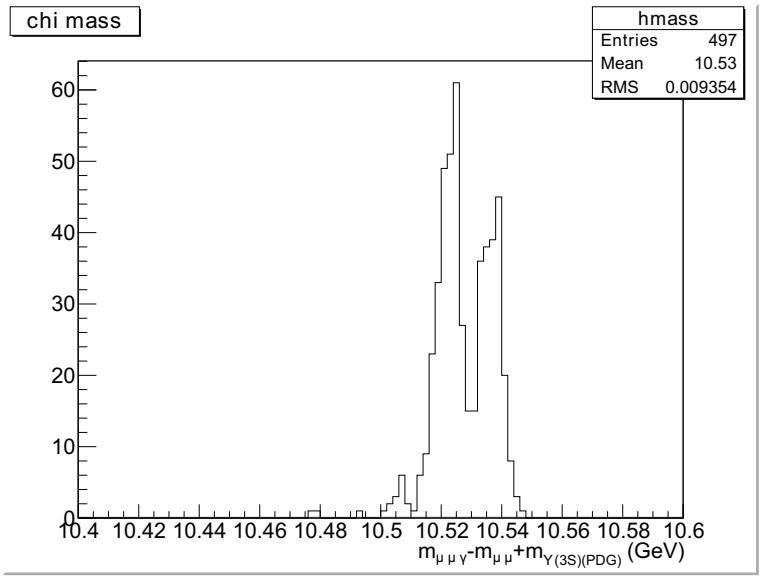

(b)

Figure 4.7: Invariant mass distributions for the recostructed $\Upsilon(3S)$ (a) and $\chi_b(3P)$ (b) from the particle gun.

4.4 Data Analysis

To extract the number of $\Upsilon^{inc}(3S)$(of the fraction of $\Upsilon(3S)$ originating from the $\chi_b(3P)$ radiative decays), it is necessary to perform an extended maximum-likelihood fit on the dimuon ($\Delta m + m_{\Upsilon,PDG}$) invariant mass spectrum.

The offline selection cuts on the dimuon pair have to be the same in both cases. Only $\mu\mu$ pairs with $|y_{\mu\mu}| < 1$ and $p_T > 9.5$ GeV are retained.

The $\Upsilon(3S)$ yield is obtained by fitting the $\mu^+\mu^-$ invariant mass distribution shown in Fig. 4.8. The Υ resonances are very narrow[3] so their lineshape is essentially due to the experimental resolution. Therefore, the signal is modeled with Crystal Ball functions (CB), probability density consisting of a Gaussian function and a power-law low-side tail. They have the analytical form:

$$f_{CB}(m) = \begin{cases} exp\left(-\frac{(m-m_0)^2}{2\sigma^2}\right) & \text{for } \frac{m-m_0}{\sigma} > -\alpha \\ \left(\frac{n}{|\alpha|}\right)^n \cdot exp\left(-\frac{|\alpha|^2}{2}\right)\left(\left(\frac{n}{|\alpha|} - \alpha\right) - \frac{m-m_0}{\sigma}\right)^{-n} & \text{for } \frac{m-m_0}{\sigma} \leq -\alpha \end{cases} \tag{4.9}$$

The resolution on the $\mu\mu$ pair, given by the σ parameter of the Gaussian part of the CB, varies linearly with rapidity, so a single CB is not sufficient to describe the experimental distribution. For this reason, the sum of two CB with the same parameters, except for the σ, is used for each peak. To describe the background, a second-degree polynomial is used.

The number of inclusive $\Upsilon(3S)$ in obtained integrating the corresponding fit function in the fixed mass range $[10.2, 10.6]$ GeV. The estimated number of $\Upsilon^{inc}(3S)$ in the selected kinematic region is

$$N\left(\Upsilon^{inc}(3P)\right) = (4.301 \pm 0.004) \cdot 10^5 \tag{4.10}$$

where the statistical error is reported.

To count the number of 3P candidates, as previously stated, the extended maximum likelihood fit has been performed on the $\Delta m + m_{\Upsilon(3S),PDG}$ distribution shown in Fig.4.9. To match the inclusive Υ selection cuts, only the $\Upsilon(3S)$ in the range $[10.2, 10.6]$ GeV are retained to build the χ_b candidates.

[3] $\Gamma(\Upsilon(1S)) = 54.02 \pm 1.25$ keV, $\Gamma(\Upsilon(2S)) = 31.98 \pm 2.63$ keV, $\Gamma(\Upsilon(3S)) = 20.32 \pm 1.85$ keV [1].

The $\chi_b(3P)$ signal is modeled with two single-sided Crystal Ball functions, one for $J = 1$ and one for $J = 2$. A fit to the reconstructed $\chi_{b1}(3P)$ and $\chi_{b2}(3P)$, obtained from the Monte Carlo sample created to study the photon reconstruction efficiency, allowed to fix the parameters. The two peaks are fitted separately, and the result is shown in Figure 4.10.

The ratio between $J = 2$ and $J = 1$ peaks is unknown, so a test value of 0.5 was used. The background is fitted with the following function:

$$g(m) = (m - q_0)^{\alpha_1} \cdot e^{(m-q_0)\cdot\beta_1} \tag{4.11}$$

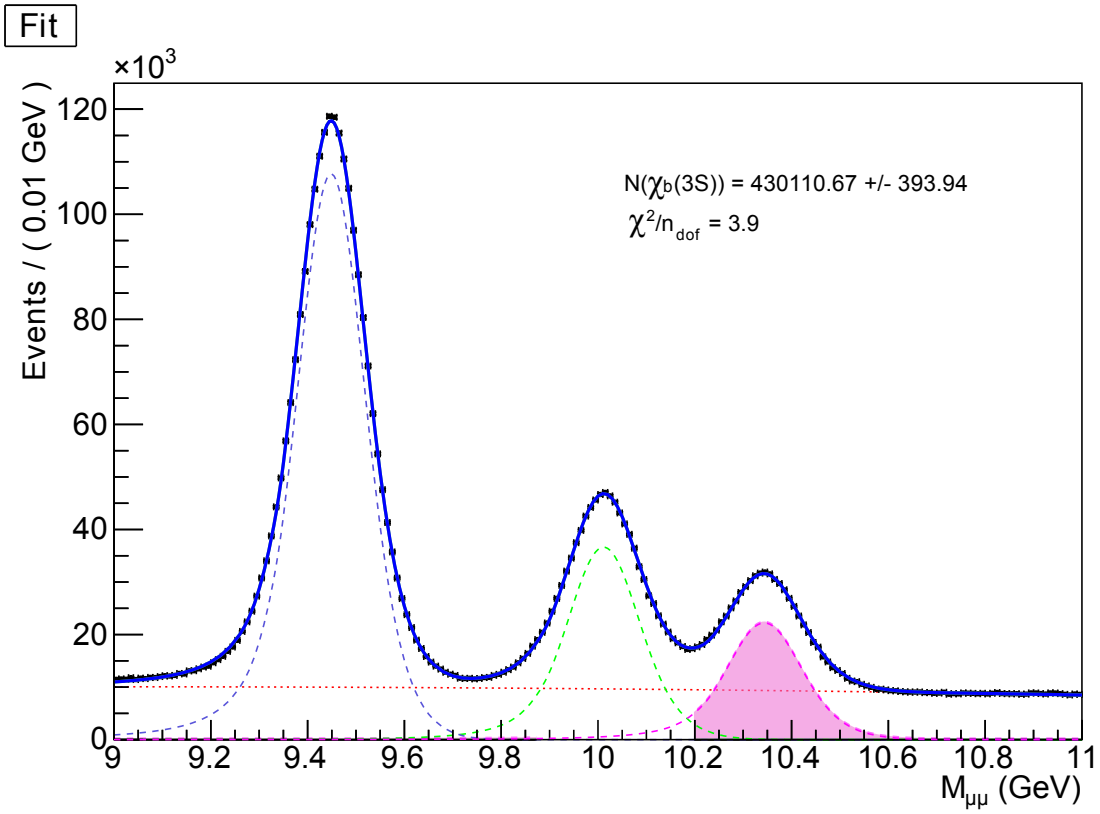

Figure 4.8: Extended maximum likelihood fit to the dimuon mass spectrum. The black points are the experimental data. Blue dashed line: fit to the $\Upsilon(1S)$ peak. Green dashed line: fit to the $\Upsilon(2S)$ peak. Pink dashed line: fit to the $\Upsilon(3S)$ peak. Red dotted line: polynomial fit to the background. The blue solid line is the global fit. The pink-shaded area specifies the range used for the $\Upsilon^{inc}(3S)$ count.

The estimated yield for $\chi_{b1,2}(3P)$ in the selected kinematic region is

$$N(\chi_{b1,2}(3P) \to \Upsilon(3S) + \gamma) = 17 \pm 5 \tag{4.12}$$

where the statistical error is reported.

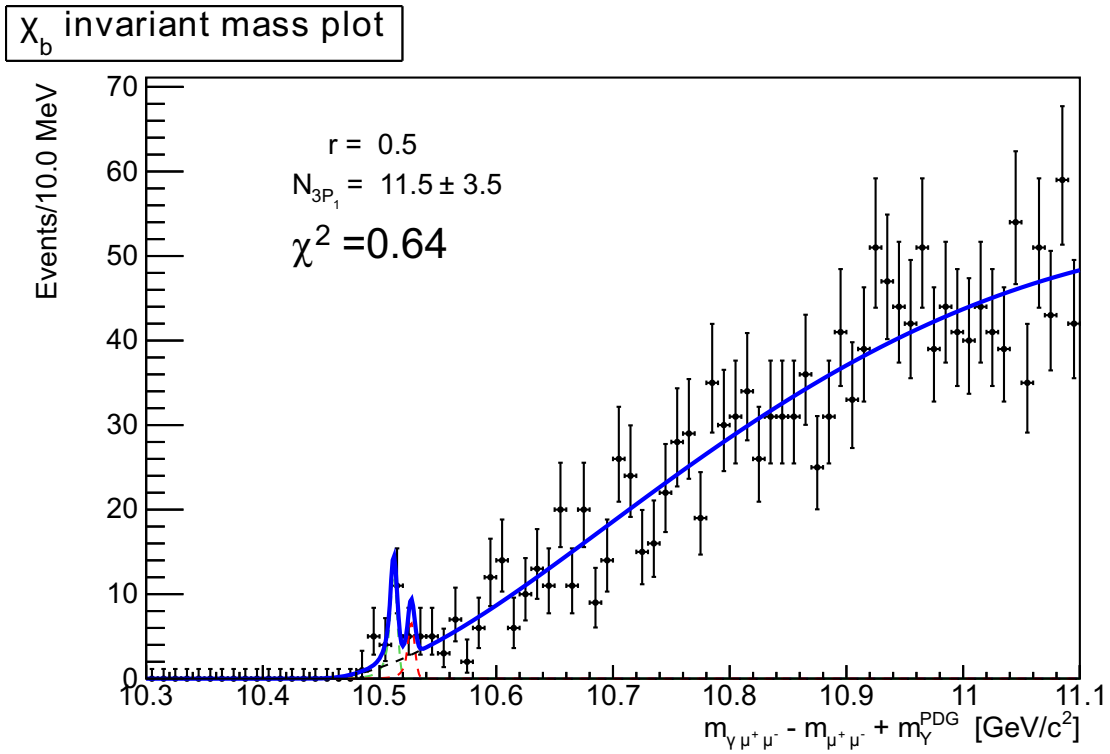

Figure 4.9: Extended maximum likelihood fit to the $\Delta m + m_{\Upsilon(3S),PDG}$ spectrum. The green dashed line corresponds to the $J = 1$ state, the red dashed line to the $J = 2$ state.

All the cuts used for the data analysis are reported in Table 4.1

Dimuon selection cuts	
muon hits in tracker	≥ 10
muon hits in pixel	≥ 2
d_0 and z_0	3 cm(r) $\times$15 cm(z)
track fit $\chi^2/n_{d.o.f.}$	< 1.8
$\mu^+\mu^-$ vertex fit probability	> 0.01
$p_{T,\mu\mu}$	> 9.5 GeV
$\lvert y(\mu^+\mu^-)\rvert$	< 1.0
$m_{\mu^+\mu^-}$	$[10.2, 10.6]$ GeV
Photon selection cuts	
Electron track fit $\chi^2/n_{d.o.f.}$	< 10
Distance of approach	-0.25 cm $< d_{xy} < 1$ cm
e^+e^- vertex fit probability	$> 5 \times 10^{-4}$
Radius of conversion	> 1.5 cm
χ_b selection	
π^0 rejection	$\lvert m_{\gamma\gamma} - m_{\pi^0,PDG}\rvert > 25$ MeV
$\Upsilon - \gamma$ vertex compatibility	5σ

Table 4.1: Summary of the selection cuts used for the data analysis.

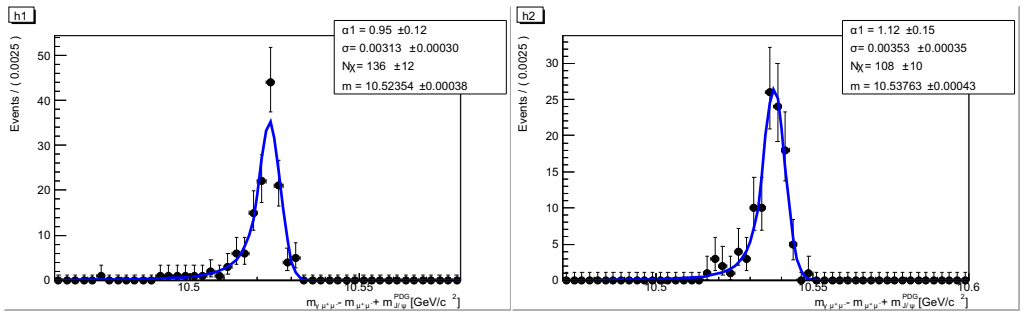

(a) (b)

Figure 4.10: Fit to the $\chi_{b1}(3P)$ (a) and $\chi_{b2}(3P)$ (b) invariant mass distributions obtained from the reconstructed events of the particle gun.

4.5 Systematic uncertainties

All the errors associated to fits are statistical only. It is fundamental to take into account that every hypotesis on unknown quantities and every approximation introduce a potential source of systematic uncertainties.

J=2 / J=1 Ratio The counting of the $\chi_b(3P)$ candidates (see 4.4) is based on the assumption that the ratio between the contribution of the two spin states $J = 2/J = 1$ can be taken equal to 0.5. The real value is influenced by the Branching Ratio for the decay channel under examination, and by the production ratio between the two states. Both this quantities are unknown and can only be estimated drawing a parallel between $\chi_b(3P)$ and $1P$–$2P$ cases (in reference to the BR), or between chi_b and chi_c (in reference to the production ratio). In order to estimate the systematic uncertainty introduced by the choice for the ratio, can be expedient to fix the ratio to different values, permitting an evaluation of how much the number of $\chi_b(3P)$ is affected by the chosen value.

For this reason the fit to the $\Delta m + m_{\Upsilon(3S),PDG}$ distribution has been repeated with r(ratio)= 0.4 and $r = 0.6$. The results are reported in Table 4.2 and shown in Figure 4.11. The results are compatible with the one obtained with $r = 0.5$. Thus, the uncertainty in the valuation of the ratio doesn't contribute to the systematic error.

	$r = 0.4$	$r = 0.5$	$r = 0.6$
$N(\chi_b(3P))$	17 ± 5	17 ± 5	16 ± 2

Table 4.2: Number of $\chi_b(3P)$ obtained from the fit to the $\Delta m + m_{\Upsilon(3S),PDG}$ distribution using different values for the ratio r $J = 2/J = 1$. The gray column corresponds to the values used in the data analysis.

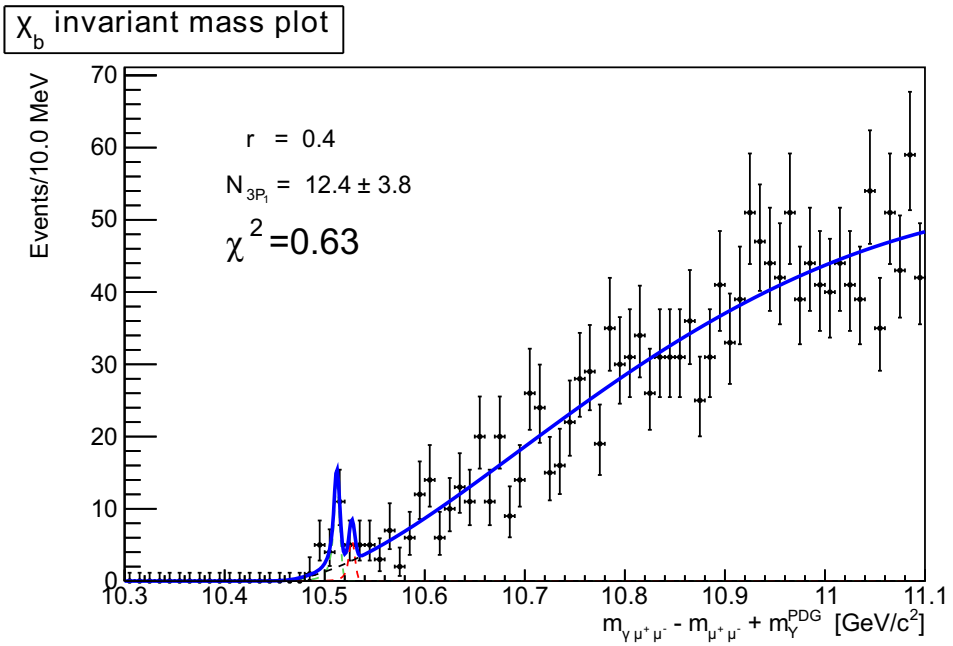

(a)

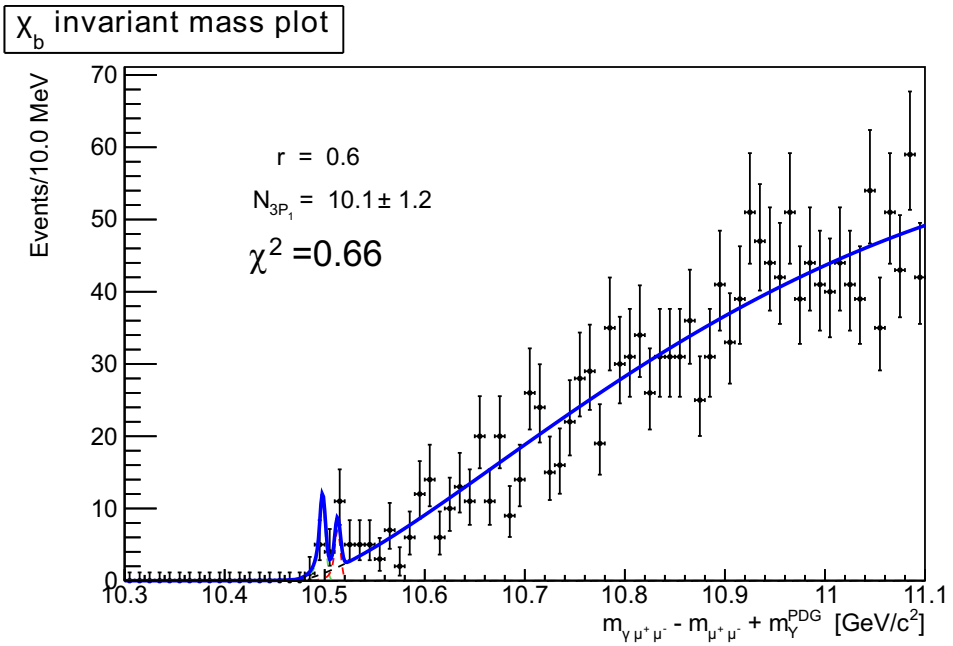

(b)

Figure 4.11: Extended maximum likelihood fit to the $\Delta m + m_{\Upsilon(3S),PDG}$ spectrum with two different choices for the ratio $J = 2/J = 1$: $r = 0.4$ (a) and $r = 0.6$ (b).

4.6 Results on $\chi_{b1,2}(3P)$ Feed-Down To $\Upsilon(3S)$

The final result for the $\chi_b(3P)$ feed-down to the $\Upsilon(3S)$ is

$$\frac{\sigma\left(\chi_b(3P) \to \Upsilon(3S) + \gamma\right)}{\sigma\left(\Upsilon^{inc}(3S)\right)} = (10.3 \pm 3.1)\% \tag{4.13}$$

obtained substituting the values 4.8, 4.10 and 4.12 into the 4.4.

This result doesn't include all the possible systematic uncertainties; nevertheless, they are not expected to be greater than statistical errors.

Chapter 5

Conclusions

The production of $\Upsilon(3S)$ and $\chi_b(3P)$ mesons observed in this work corresponds to approximately the whole data set collected by the CMS experiment in pp collisions at a centre-of-mass energy of 8 TeV. This preliminary work has not considered all the possible systematic uncertainties; most of all, those relative to the determination of the photon reconstruction efficiency, which has been calculated in a simple way indeed. Nevertheless, the systematic uncertainties are not expected to be greater than statistical errors. The feed-down of $\chi_b(3P)$ to $\Upsilon(3S)$ in the kinematic range $|y_\Upsilon| < 1.0$, $p_{T,\Upsilon} > 9.5$ GeV and $p_{T,\gamma} > 0.5$ GeV is measured to be

$$(10.3 \pm 3.1)\% \tag{5.1}$$

where the error concerns the statistic uncertainty. The fraction of $\Upsilon(3S)$ originating from the $\chi_b(3P)$ decays is thus a significant part of $\Upsilon(3S)$ produced in pp collisions. This fact can be of fundamental importance for polarization and production cross section future studies.

Appendix A

χ_b invariant mass distribution for different decay channels

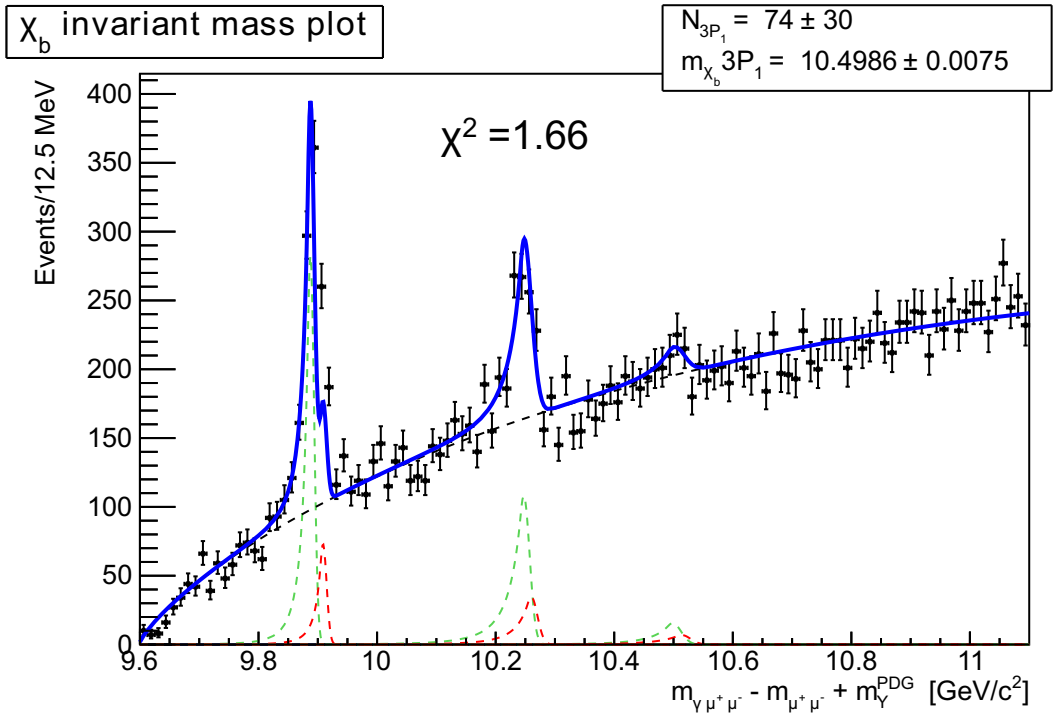

Figure A.1: Mass distribution of $\chi_b \to \Upsilon(1S)\gamma$. The green dashed line corresponds to the $J = 1$ state, the red dashed line to the $J = 2$ state.

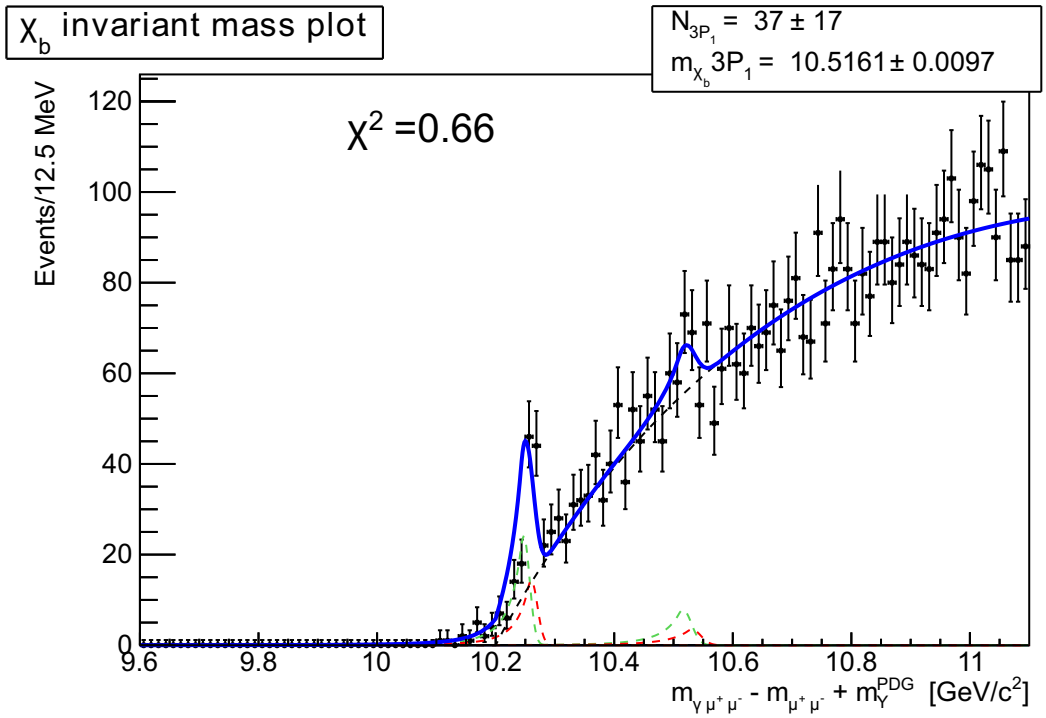

Figure A.2: Mass distribution of $\chi_b \to \Upsilon(2S)\gamma$. The green dashed line corresponds to the $J = 1$ state, the red dashed line to the $J = 2$ state.

Appendix B

Relevant distributions obtained from Monte Carlo simulation

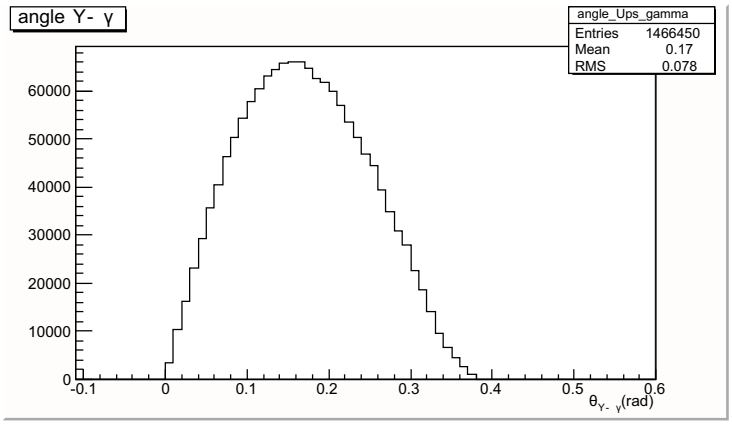

Figure B.1: Angle between $\Upsilon(3S)$ and γ direction at generation in the Monte Carlo simulation, for $|y_\Upsilon| < 1.0$ and $p_{T,\gamma} > 0.5$ GeV.

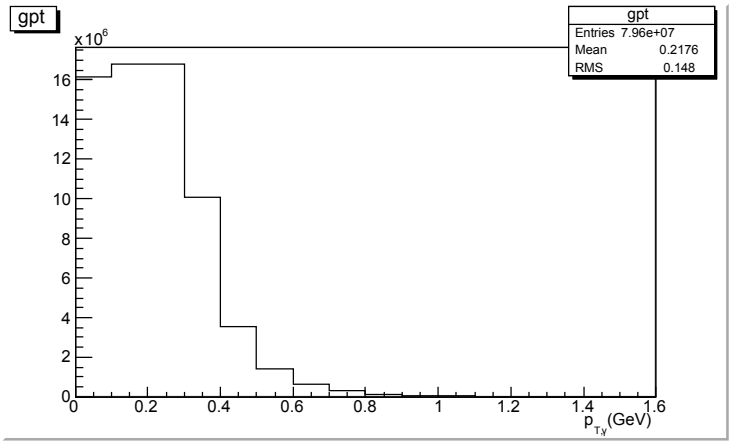

Figure B.2: Transverse momentum distribution for generated photons in the Monte Carlo simulation, without acceptance cuts.

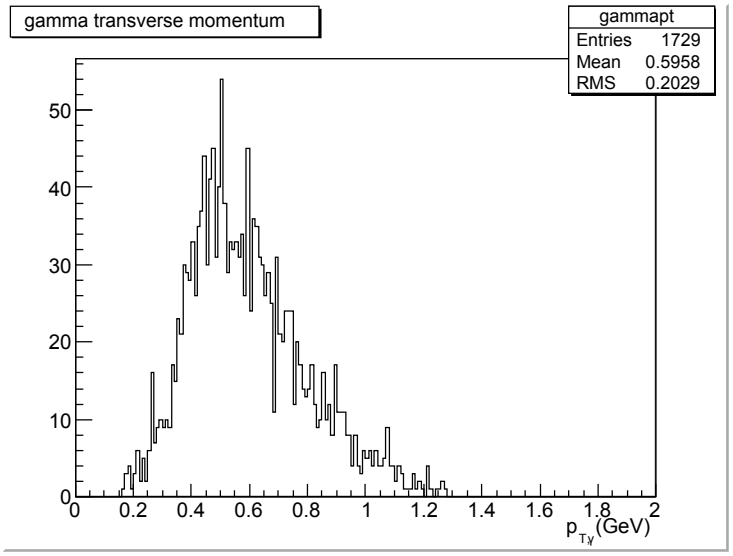

Figure B.3: Transverse momentum distribution for reconstructed photons in the Monte Carlo simulation, without acceptance cuts.

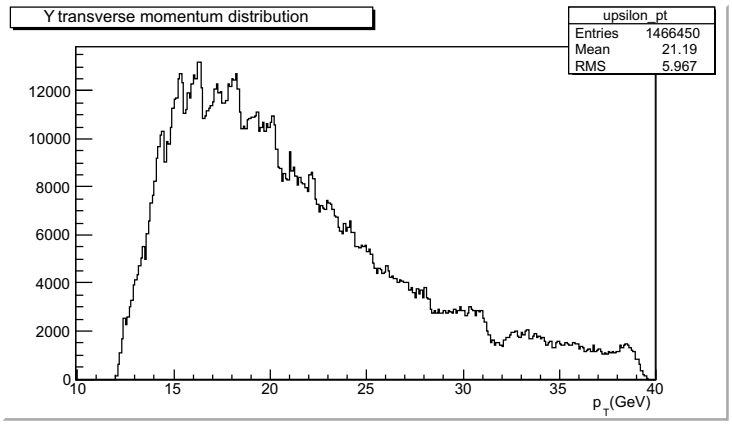

Figure B.4: Transverse momentum distribution for generated $\Upsilon(3S)$ in the Monte Carlo simulation, for $|y_\Upsilon| < 1.0$ and $p_{T,\gamma} > 0.5$ GeV.

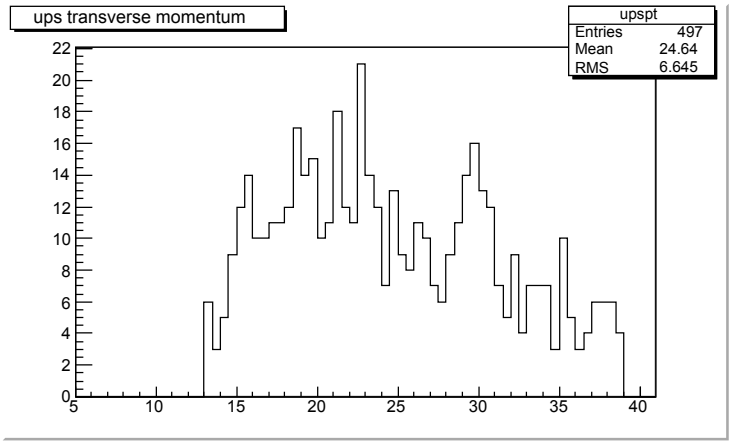

Figure B.5: Transverse momentum distribution for reconstructed $\Upsilon(3S)$ in the Monte Carlo simulation, for $|y_\Upsilon| < 1.0$ and $p_{T,\gamma} > 0.5$ GeV.

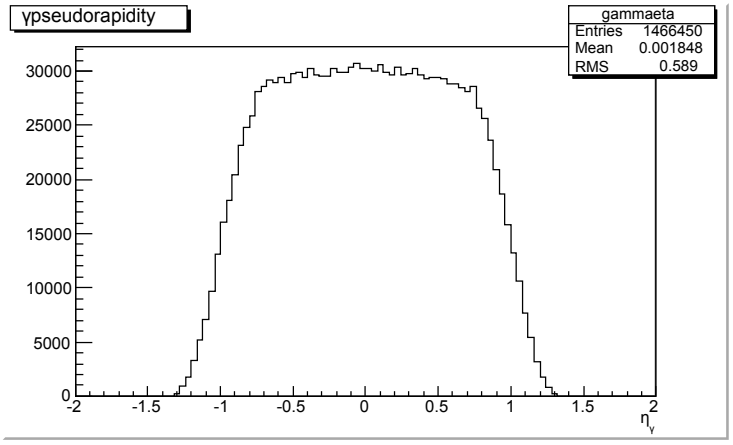

Figure B.6: η distribution for generated photons in the Monte Carlo simulation, for $|y_\Upsilon| < 1.0$ and $p_{T,\gamma} > 0.5$ GeV.

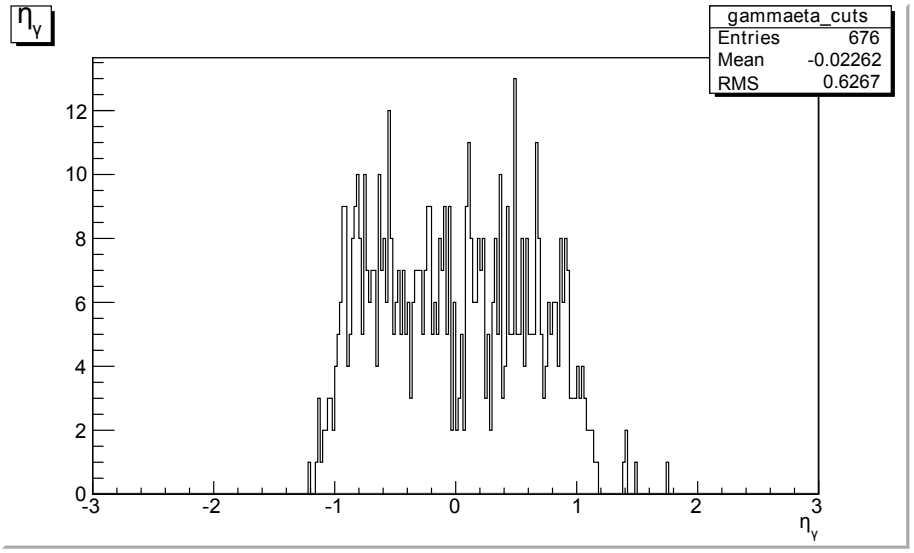

Figure B.7: η distribution for reconstructed photons in the Monte Carlo simulation, for $|y_\Upsilon| < 1.0$ and $p_{T,\gamma} > 0.5$ GeV.

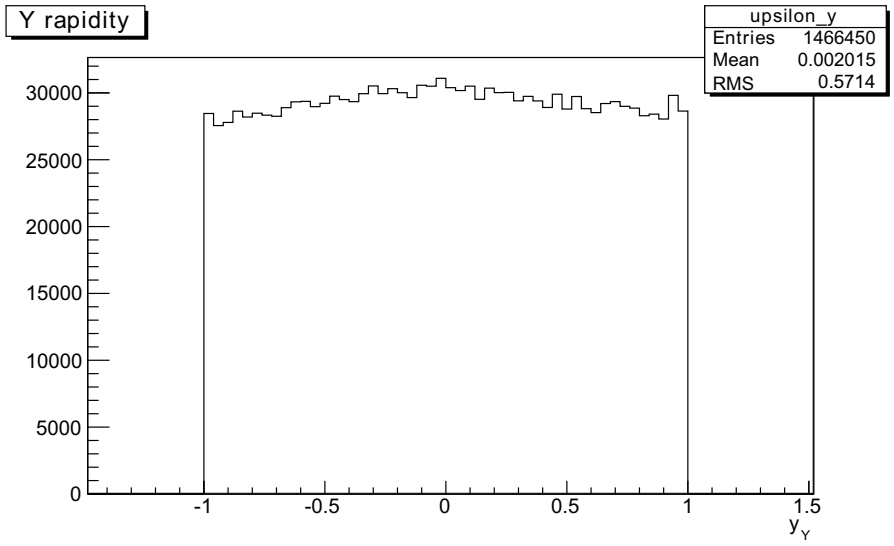

Figure B.8: y distribution for reconstructed $\Upsilon(3S)$ in the Monte Carlo simulation, for $|y_\Upsilon| < 1.0$ and $p_{T,\gamma} > 0.5$ GeV.

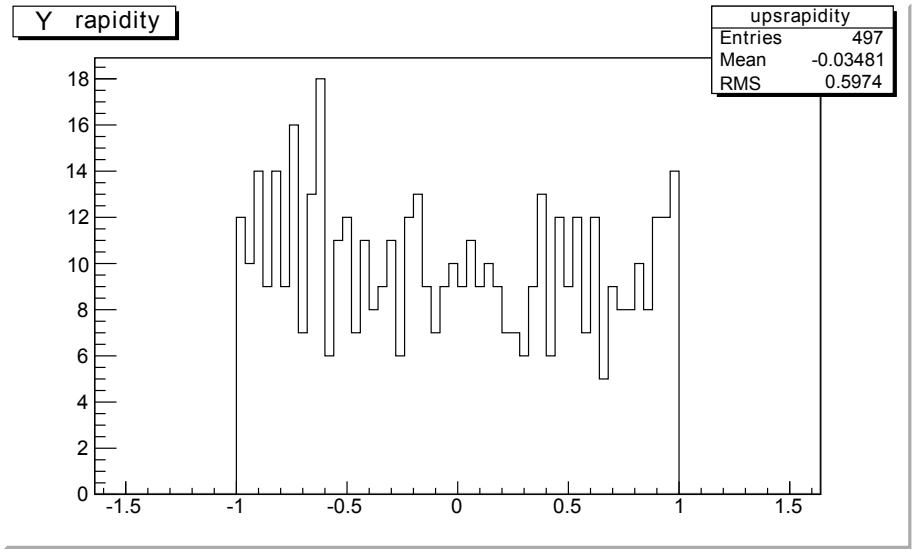

Figure B.9: y distribution for reconstructed $\Upsilon(3S)$ in the Monte Carlo simulation, for $|y_\Upsilon| < 1.0$ and $p_{T,\gamma} > 0.5$ GeV.

Bibliography

[1] J. Beringer *et al.*, (Particle Data Group), *Phys. Rev. D86, 010001* (2012).

[2] D.Griffiths, *Introduction to Elementary Particles* (1987).

[3] N. Brambilla *et al.*, *Heavy quarkonium: progress, puzzles, and opportunities*, arXiv:hep-ph/1010.5827 (2011).

[4] The ATLAS Collaboration, *Observation of a new χ_b state in radiative transitions to $\Upsilon(1S)$ and $\Upsilon(2S)$ at ATLAS*, *CERN-PH-EP-2011-225* (2011).

[5] The D0 Collaboration, *Observation of a narrow mass state decaying into $\Upsilon(1S)+\gamma$ in $p\overline{p}$ collisions at $\sqrt{s} = 1.96\ TeV$*, arXiv:hep-ex/1203.6034v1 (2012).

[6] The CMS collaboration, *The CMS experiment at CERN LHC* (2008) JINST 3. S08004.http://iopscience.iop.org/1748-0221/3/08/S08004

[7] The CMS collaboration, *Detector performance and software, physics technical design report*, vol. 1. *CERN/LHCC 2006-001, CMS TDR 8.1* (2006).

[8] The CMS collaboration, *The TriDAS project, technical design report*, vol 2: Data acquisition and high-level trigger technical design report, *CERN-LHCC-2002-026*, http://cdsweb.cern.ch/record/578006.

[9] The CMS collaboration, *Studies of tracker material*, *CMS-PAS-TRK-10-003* (2010).

[10] The CMS collaboration, *Measurement of the relative prompt production rate of χ_{c2} and χ_{c1} in pp collisions at $\sqrt{s} = 7\ TeV$*, arXiv:hep-ex/1210.0875, (2012).

[11] H. K. Wöhri *et al.*, *Low p_T Muon and Dimuon Efficiencies*, *CMS AN AN-12-088* (2012).

[12] C. O. Dib, N. Neill, *$\chi_b(3P)$ splitting predictions in potential models*, arXiv:hep-ph/1208.2186v1 (2012).

[13] The CMS Collaboration, *Measurement of the $\Upsilon(nS)$ cross-section in pp collisions at $\sqrt{s} = 7\ TeV$*, *CMS BPH-11-001* (2012).